

## A Bright Future for Engineering Piezoelectric 2D Crystals

Peter. C. Sherrell<sup>a,\*</sup>, Marco Fronzi<sup>b,c,†</sup>, Nick A. Shepelin<sup>a,d</sup>, Alexander Corletto<sup>a,e</sup>, David Winkler<sup>f,g,h</sup>, Mike Ford<sup>b</sup>, Joseph G. Shapter<sup>e</sup>, and Amanda V. Ellis<sup>a,\*</sup>

Received 00th January 20xx,  
Accepted 00th January 20xx

DOI: 10.1039/x0xx00000x

The piezoelectric effect, mechanical-to-electrical and electrical-to-mechanical energy conversion, is highly beneficial for functional and responsive electronic devices. To fully exploit this property, miniaturization of piezoelectric materials is the subject of intense research. Indeed, select atomically thin 2D materials strongly exhibit the piezoelectric effect. The family of 2D crystals consists of over 7000 chemically distinct members that can be further manipulated in terms of strain, functionalization, elemental substitution (i.e. Janus 2D crystals), and defect engineering to induce a piezoelectric response. Additionally, most 2D crystals can stack with other similar or dissimilar 2D crystals to form a much greater number of complex 2D heterostructures whose properties are quite different to those of the individual constituents. The unprecedented flexibility in tailoring 2D crystal properties, coupled with their minimal thickness, make these emerging highly attractive for advanced piezoelectric applications that include pressure sensing, piezocatalysis, piezotronics, and energy harvesting. This review summarizes literature on piezoelectricity, particularly out-of-plane piezoelectricity, in the vast family of 2D materials as well as their heterostructures. It also describes methods to induce, enhance, and control the piezoelectric properties. The volume of data and role of machine learning in predicting piezoelectricity is discussed in detail, and a prospective outlook on the 2D piezoelectric field is provided.

### 1. Introduction

The highly anisotropic nature of two dimensional (2D) materials means that straining the lattice,<sup>1</sup> inducing defects,<sup>2</sup> or even adsorbing atoms<sup>3</sup> onto the surface can result in dramatic changes in their physical and electronic properties. These properties can be further manipulated by van der Waals (vdW) stacking<sup>4</sup> of discrete 2D components to produce heterodimers and heterooligomers, unlocking an even wider range of properties for next generation applications.<sup>5</sup> An emerging research focus of particular interest is the piezoelectric properties of 2D crystals, that is the interconversion between mechanical and electrical energy.

2D crystals are already widely studied for catalytic<sup>6</sup> and photonic applications,<sup>7</sup> and the coupling between piezoelectric output and these phenomena (e.g., piezo-catalysis, piezo-photo-catalysis, piezo-tronics and piezo-phototronics) leads to dramatic improvements in device performance by lowering energy barriers.<sup>8</sup> However, since most 2D crystals do not exhibit strong intrinsic piezoelectric effects, atomic scale engineering approaches are needed to induce or enhance piezoelectric properties to exploit these materials.

This review introduces the fundamentals of piezoelectricity, including key parameters and figures of merit. Subsequently we discuss how piezoelectricity has been observed in 2D crystals, with a focus on homostructures (that is single- and multi-layered 2D crystals made from a single materials). Then, ways of engineering, enhancing, and exploiting piezoelectricity are explored including chemical modification, and heterostructure formation. We then discuss machine learning methods that enable the accurate prediction of piezoelectric coefficients for the vast family of 2D crystals and their heterostructures. The broad focus of the review enables us to provide guidance for material selection and to give a perspective on the future of the field.

Before discussing piezoelectricity in 2D crystals, it is first necessary to understand the origin of the piezoelectric effect. To exhibit piezoelectric properties, a material must have a non-centrosymmetric unit cell producing an anisotropic dipole moment, otherwise known as polarization.<sup>9</sup> Dipolar anisotropy is most commonly observed in crystalline and semicrystalline dielectric materials due to their organized structures and ability

<sup>a</sup> Department of Chemical Engineering, The University of Melbourne, Parkville, Victoria, 3010, Australia

<sup>b</sup> School of Mathematical and Physical Science, University of Technology Sydney, Ultimo, New South Wales, 2007, Australia

<sup>c</sup> Shibaura Institute of Technology, SIT Research Laboratories, 3-7-5, Toyosu, Koto-ku, Tokyo, 135-8548, Japan

<sup>d</sup> Laboratory for Multiscale Materials Experiments, Paul Scherrer Institut, CH-5232 Villigen, Switzerland

<sup>e</sup> Australian Institute for Bioengineering and Nanotechnology, The University of Queensland, Brisbane, Queensland, 4072, Australia

<sup>f</sup> Monash Institute of Pharmaceutical Sciences, Monash University, 381 Royal Parade, Parkville, Victoria 3052, Australia

<sup>g</sup> School of Biochemistry and Genetics, La Trobe Institute for Molecular Science, La Trobe University, Kingsbury Drive, Bundoora, Victoria 3086, Australia

<sup>h</sup> School of Pharmacy, The University of Nottingham, Nottingham NG7 2RD, UK

<sup>†</sup> Denotes equal contribution

\*PCS: [peter.sherrell@unimelb.edu.au](mailto:peter.sherrell@unimelb.edu.au)

\*MF: [m-fronzi@shibaura-it.ac.jp](mailto:m-fronzi@shibaura-it.ac.jp)

\*AVE: [amanda.ellis@unimelb.edu.au](mailto:amanda.ellis@unimelb.edu.au)

to be polarized under external electric fields ( $E_i$  where  $i$  corresponds to the vector direction in three-dimensional space). Notably, most dielectric materials exhibit a linear dielectric response to an applied  $E_i$  and are thus isotropic at  $E_i = 0$  (Figure 1a). Starting at the origin (Figure 1a), and following path 1, the dipole moments of crystallites align with increasing applied  $E_i$ . With decreasing  $E_i$  (path 2) the dielectric material crosses through the origin and before having a flipped polarization at a negative applied  $E_i$  (path 3). Upon returning to  $E_i = 0$  (path 4), the dielectric is at a neutral state, and will not exhibit any polarization. In contrast, ferroelectric materials retain polarization in the absence of an external field (Figure 1b). Here, starting from the origin (path 1), dipole ordering increases up to a given applied  $E_i$ . This polarization under an applied  $E_i$  is called the spontaneous polarization ( $P_s$ ). When the  $E_i$  returns to 0 (path 2), the ferroelectric material remains partially polarized, a phenomenon known as remnant polarization ( $P_r$ ). With continued sweeping of  $E_i$  (paths 3 through 7), the ferroelectric will reversibly cycle through a hysteresis loop. It is the existence of the  $P_r$  (i.e., stable polarization) that allows piezoelectric phenomena in conventional ferroelectrics.

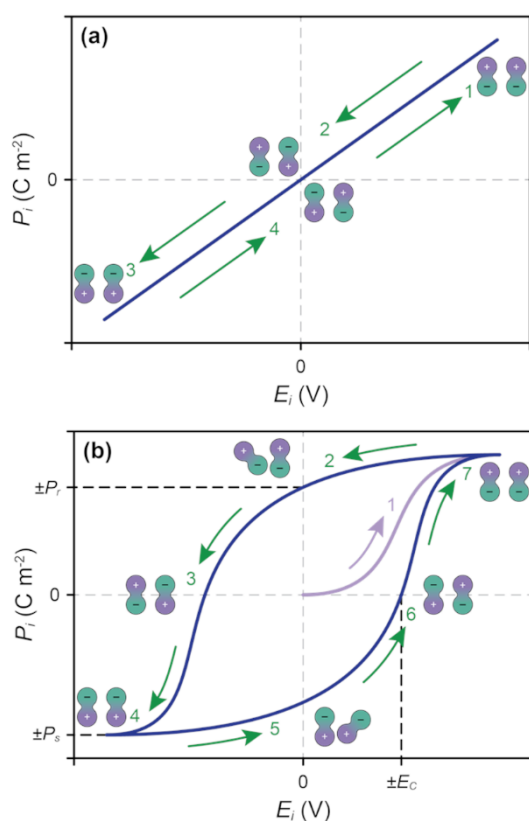


**Figure 1.** The conventional relationship between the applied electric field ( $E_i$ ) and the resultant polarization ( $P_i$ ) in; (a) linear dielectric materials and; (b) ferroelectric materials. Linear dielectric materials in (a) undergo spontaneous dipolar orientation with applied  $E_i$ , subsequently returning to a randomized dipolar orientation in the absence of applied  $E_i$ . Ferroelectric materials in (b) undergo a similar dipolar orientation when the magnitude of the applied  $E_i$  is greater than the coercive field ( $E_c$ ) of the material and the  $P_i$  saturates at the spontaneous polarization ( $P_s$ ) of the material. Following the removal of the  $E_i$ , the dipolar orientation reduces via relaxation to the remnant polarization ( $P_r$ ) value.

The  $i$  vector, corresponding to the direction of the applied electric field, can induce various electrochemical effects depending on the dipolar anisotropy of a given unit cell. The most commonly studied systems are the  $11$  system (applied electric field in the x-direction, mechanical response in the x-direction, Figure 2a), the  $31$  system (applied electric field in the z-direction, mechanical response in the x-direction, Figure 2b), and the  $33$  system (applied electric field in the z-direction, mechanical response in the z-direction, Figure 2c). It should be noted that mechanical response and electric response are interchangeable in their directions and effects. For 2D crystals, the  $11$  system is considered in-plane piezoelectric response, whereas  $31$  and  $33$  are considered out-of-plane (OOP) piezoelectric response.

The piezoelectric effect efficiently and reversibly converts between mechanical and electrical energies. The electromechanical coupling is described by the coupling of the mechanical (stress-strain) and dielectric (electric displacement-electric field) constitutive equations (Equation 1a and 1b), shown without the tensor notation for simplicity.<sup>10</sup>

$$S = sT + dE \quad 1a$$

$$D = dT + \epsilon E \quad 1b$$

In Equation 1a, the induced mechanical strain ( $S$ ) is related to the applied stress ( $T$ ) via Young's modulus ( $s$ ), and to the applied electric field ( $E$ ) via the charge form of the piezoelectric coefficient ( $d$ ), demonstrating the influence of the electric field on strain in electromechanically coupled materials. Conversely, in Equation 1b, the induced electric displacement ( $D$ ) is related to the applied stress,  $T$ , by the  $d$  coefficient, and to the applied electric field,  $E$ , by the dielectric constant ( $\epsilon$ ). Notably, the electric displacement (i.e., spatial separation of bound surface charges), is directly proportional to the polarization. As a result, an electric field applied to a polarized material will induce an internal strain (i.e., dimensional expansion or contraction), and applied stress will induce an electric displacement field and thus a measurable charge. These coupling phenomena are demonstrated in Figure 2a and Figure 2b for Equation 1a, and in Figure 2c for Equation 1b, respectively.

The piezoelectric coefficients are dependent on the stimulus and the measured quantity; thus, it is useful to define two critical parameters that will be discussed in this review. As shown in Equations 1a and 1b, the coupling coefficient between the strain and electric field and the displacement field and stress is the piezoelectric charge coefficient,  $d$ . This coefficient can be obtained by either measuring mechanical strain under an applied electric field (Equation 2a) or measuring the displacement field (via short circuit charge) under an applied mechanical stress (Equation 2b), with the boundary condition of constant stress or constant electric field, respectively. The units are given in  $\text{m V}^{-1}$  in Equation 2a and  $\text{C N}^{-1}$  for Equation 2b.

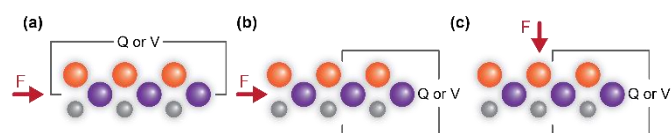


**Figure 2.** Schematic of the three main modes measured for piezoelectric output; (a) the 11 mode, where force (typically longitudinal strain) is applied in plane, parallel to the measured charge or voltage; (b) the 31 mode, where force is applied longitudinally and charge or voltage is measured out-of-plane; and (c) the 33 mode where compressive force is applied out-of-plane and charge or voltage is measured out of plane.

$$d_{ij} = \left( \frac{\partial S_j}{\partial E_i} \right)_T \quad 2a$$

$$d_{ij} = \left( \frac{\partial D_i}{\partial T_j} \right)_E \quad 2b$$

An alternative form that will be used throughout this review is the piezoelectric stress coefficient,  $e$ . In this form, the coefficient relates either an induced stress to an applied electric field at constant strain (Equation 3a), or an induced displacement field to an applied strain at constant electric field (Equation 3b). The units for the following forms are given as  $\text{N V}^{-1}$  for Equation 3a and  $\text{C m}^{-2}$  for Equation 3b. In both forms of the piezoelectric coefficient,  $i$  and  $j$  represent the direction used for either the application of a stimulus or the measurement of the effect, with  $i$  between 1 and 3, and  $j$  between 1 and 6 (to account for the shear modes). The values of 1, 2 and 3 are used to map directly to the directions of the crystallographic  $a$ ,  $b$  and  $c$  axes of the material studied.

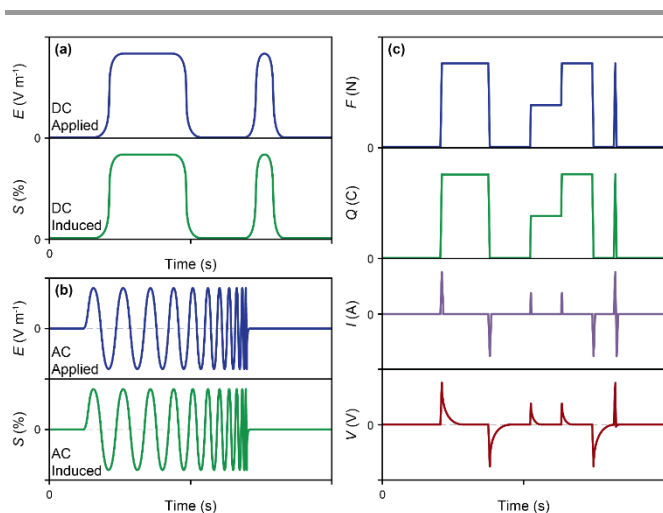


**Figure 3.** Demonstration of the principle of piezoelectric coupling; (a) the application of a DC bias and the subsequent expansion of a piezoelectric material through the converse piezoelectric effect; (b) the application of an AC bias, demonstrating the frequency dependent expansion and contraction of a piezoelectric material through the converse piezoelectric effect; (c) the application of a mechanical force ( $F$ ) and the influence on the surface charge ( $Q$ ), generated current ( $I$ ) and generated voltage ( $V$ ) profiles of a piezoelectric material through the direct piezoelectric effect.

$$e_{ij} = \left( \frac{\partial T_j}{\partial E_i} \right)_S \quad 3a$$

$$e_{ij} = \left( \frac{\partial D_i}{\partial S_j} \right)_E \quad 3b$$

This electromechanical coupling results in the converse piezoelectric effect (whereby an electric field is applied, and a strain ( $S$ ) is induced) having minimal time lag in both direct current (DC) and alternating current (AC modes) (Figure 3a, b). However, the direct piezoelectric effect (applied force and resultant charge, current, voltage measurement) has a time dependence (Figure 3c), due to the measured current and voltage corresponding to the rate of change of deformation for the piezoelectric material. This time dependence typically leads to extremely short voltage and current spikes that are not accurately measured by many measurement devices, leading to misreporting of piezoelectric data.<sup>11</sup>

To understand how these direct and converse piezoelectric effects in- and out-of-plane operate in real materials, we must look at crystal structures. In bulk piezoelectric materials, the piezoelectric effect arises from the spatial displacement of atomic charges within the unit cell (e.g., the out-of-plane (OOP) divalent titanium ions ( $\text{Ti}^{2+}$ ) displacement in lead titanate ( $\text{PbTiO}_3$ ), shown in Figure 4a). This is the case for  $\text{PbTiO}_3$  with the thickness at one unit cell (Figure 4a), or germanium telluride ( $\text{GeTe}$ ) nanosheets,<sup>12</sup> where the vertical separation of the Ge and Te atoms induces piezoelectricity in the OOP direction, perpendicular to the basal plane (Figure 4b). Such distorted 2D structures are also capable of exhibiting in-plane piezoelectricity. Conversely, monolayers of planar 2D crystals, and distorted structures with symmetry along the OOP direction, are unable to achieve OOP polarization so are limited to in-plane piezoelectricity. Examples of these are graphene nitride ( $\text{C}_3\text{N}_4$ ,<sup>13</sup> Figure 4c) and molybdenum sulfide ( $\text{MoS}_2$ ,<sup>14</sup> Figure 4d), respectively.

To overcome this restriction and to achieve OOP piezoelectricity, the layering of multiple different 2D crystals can be explored to break this OOP symmetry.<sup>15, 16</sup> However, many methods to achieve this result in stacking sequences that deviate from commensurate stacking, preventing observation of the piezoelectric effect (Figure 4e). The purposeful layering of multiple 2D crystals with complementary electronic properties (Figure 4f) is emerging as a powerful technique to induce OOP piezoelectricity in those materials, which are otherwise limited to in-plane polarization.<sup>17</sup> This method shows great promise for fine control of piezoelectricity. These concepts will be explored further in Section 3.

With this background in the origin of, and properties of piezoelectric phenomena, the following section describes how the piezoelectric effect is manifest in diverse classes of 2D crystals.

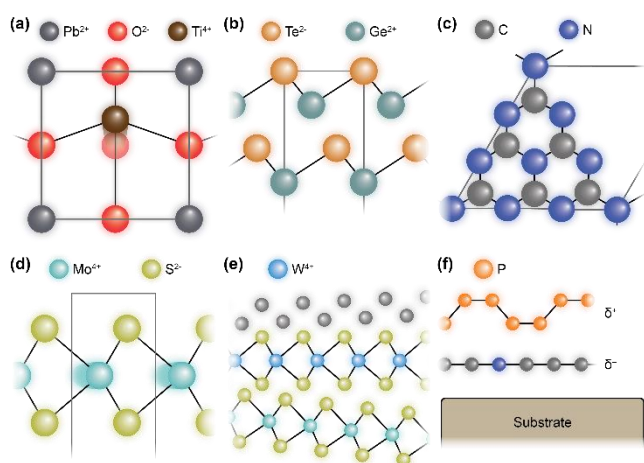


**Figure 4.** The structure of selected 2D crystals exhibiting piezoelectric properties; (a) the conventional perovskite structure  $\text{PbTiO}_3$ , shown for a thickness of one unit cell, side view; (b) the chalcogen structure  $\text{GeTe}$  in the rhombohedral  $\alpha$  phase, side view; (c) the planar  $\text{C}_3\text{N}_4$  nanosheets, top view; (d) the transition metal dichalcogenide  $\text{MoS}_2$ , side view; (e) demonstration of the non-ideal stacking arising from solution-processing; and (f) demonstration of heterostructure layering for inducing piezoelectricity.

## 2. Measurement and prediction of piezoelectricity in monolayer 2D crystals

Here we summarize individual 2D crystals of fixed atomic composition (homostructures) that have been reported to display the piezoelectric effect. While we have largely selected reports of monolayer 2D crystals, some few-layered 2D crystals are also discussed, where appropriate.

Layered 2D crystals are very attractive for energy storage, conversion, and harvesting applications due to their inherently high surface area, diverse surface chemistries, and versatility in processing and assembly. However, this diversity makes simplistic classification and understanding of the piezoelectric effect in each 2D crystal class challenging.

The fundamental piezoelectric effect, arising from dipole motion in asymmetric crystal structures, means that many 2D layered materials have little or no  $d_{33}g_{33}$  (out-of-plane piezoelectricity) and modest  $d_{31}g_{31}$  (in-plane to out-of-plane) values. However, isotropic nanoparticle vacancies in crystals that have only a small effect on the net dipole moment are likely to break the symmetry of the point group in 2D crystals and enable piezoelectric properties.<sup>2</sup>

The following section is not comprehensive, rather it summarizes published piezoelectric properties of a variety of the most studied 2D crystals.

Single atomic-layer materials can be broadly split into two categories, homoatomic (e.g., graphene, phosphorene and antimonene) or heteroatomic (e.g., hexagonal boron nitride, indium sulfide and gallium arsenide). While elemental single atomic-layer materials do not exhibit *intrinsic* out-of-plane piezoelectric effects due to their centrosymmetric nature, they

often do have in-plane piezoelectric properties, depending on the degree of ionization of their covalent bonds. This section will detail literature on piezoelectric properties of both elemental and compound single atomic-layer materials.

### a. Graphene

As the first identified 2D crystal, graphene (a zero band-gap semiconductor) has received more attention as a piezoelectric material than many other 2D crystals. It has a highly symmetrical  $D_{6h}$  crystal structure, and as such is not intrinsically piezoelectric.<sup>2, 18</sup> However, due to the exceptional mechanical strength and chemical stability of graphene, piezoelectricity can be *induced* by creating well defined pores in the basal plane,<sup>2</sup> or by biaxially straining the graphene sheet<sup>19</sup>. Wang *et al.*,<sup>19</sup> used strain engineering to demonstrate a substantial  $37 \text{ nC N}^{-1} d_{33}$  coefficient in graphene using the direct piezoelectric effect (mechanical-to electrical), while noting the converse effect (electrical-to-mechanical) was significantly lower at  $12.5 \mu\text{m V}^{-1}$ . This converse effect is significantly lower than the direct effect because of the high conductivity and large quantum capacitance of graphene that causes charge dissipation when a voltage is applied.

However, the electronic structure of graphene allows other methods, beyond defect or strain engineering, to induce piezoelectric outputs. For example, the seminal report by Ong and Reed,<sup>20</sup> showed that adsorbing atoms on the surface of graphene can generate a significant converse piezoelectric effect, up to a  $d_{31}$  of  $0.3 \text{ pm V}^{-1}$  for fluorine and lithium doped graphene. This induced piezoelectricity arises from charge transfer from the graphene to the adatoms, leading to a net dipole across the graphene sheet.<sup>20</sup>

### b. Phosphorene/Black Phosphorous

Phosphorene is an emerging 2D crystal that is intrinsically piezoelectric due to its non-centrosymmetric point group.<sup>21</sup> Moreover, its buckled structure allows it to exhibit out-of-plane piezoelectric responses. The two calculated values of the strain piezoelectric response are  $e_{11} = 59 \text{ pC m}^{-1}$  in-plane and  $e_{31}^p = 1.06 \text{ pC m}^{-1}$  out-of-plane.<sup>22</sup> The calculated in-plane piezoelectric value is comparable to that of other piezoelectric nanomaterials such as indium selenide ( $\text{InSe}$ ) ( $57 \text{ pC m}^{-1}$ ), gallium phosphide ( $\text{GaP}$ ) ( $52.6 \text{ pC m}^{-1}$ ), gallium arsenide ( $\text{GaAs}$ ) ( $49 \text{ pC m}^{-1}$ ) and fluorinated hexagonal boron nitride ( $\text{h-BN}$ ) ( $84 \text{ pC m}^{-1}$ ).<sup>3, 23</sup> The out-of-plane  $e_{31}^p$  is also comparable to some 2D buckled hexagonal compounds such as gallium antimonide ( $\text{GaSb}$ ) ( $0.8 \text{ pC m}^{-1}$ ) and indium antimonide ( $\text{InSb}$ ) ( $2.3 \text{ pC m}^{-1}$ ).<sup>23</sup>

These papers assume a 1:1 relationship between the displacement field and polarization, allowing the representation of the piezoelectric coefficient in  $\text{C m}^{-1}$ . However, units of  $\text{C m}^{-1}$  represent values of polarization, and  $\text{C m}^{-2}$  represent piezoelectric coefficients. Thus, these reports can lead to significant confusion for the broad and multidisciplinary readership of piezoelectric literature.

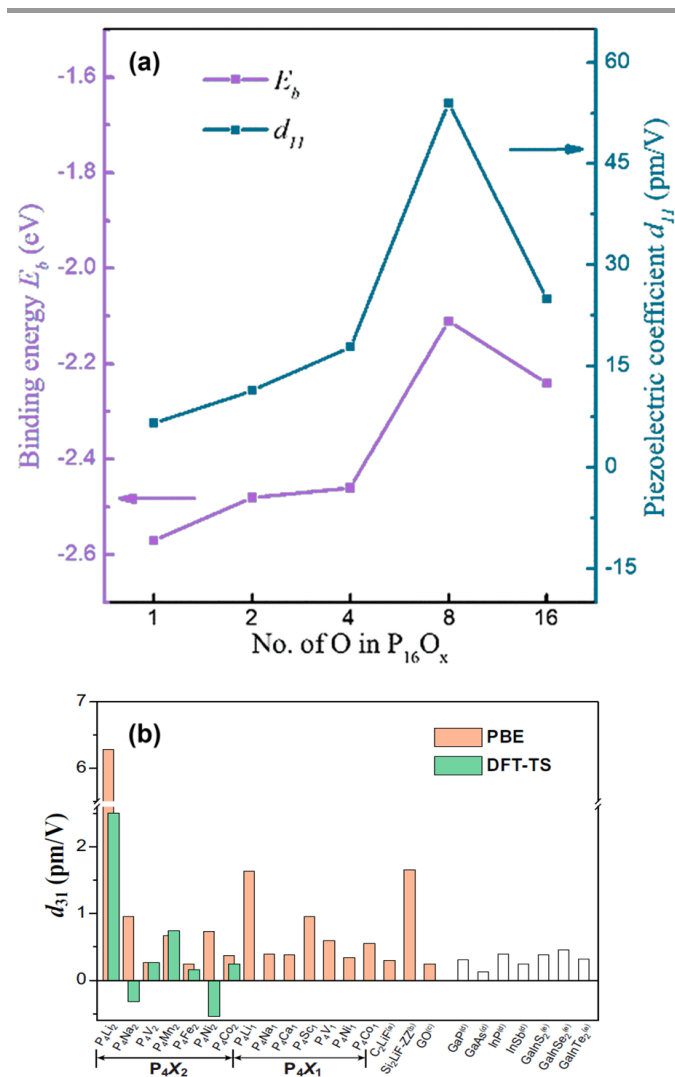


**Figure 5.** (a) Effect of oxygen doping on the piezoelectric coefficient in oxidised monolayer phosphorene oxide<sup>24</sup> (Adapted from Ref. <sup>24</sup> with permission from the Royal Society of Chemistry, Copyright 2017); and (b) comparison of piezoelectric coefficients  $d_{31}$  of an adatom-doped black P with previously known values for 2D piezoelectric materials. The orange and green bars represent values of  $d_{31}$  calculated using the PBE functional and the DFT-TS scheme, respectively. GO denotes the graphene oxide. The colour filled and unfilled bars represent adatom-induced piezoelectric materials and intrinsic piezoelectric materials, respectively. The superscript labels “(a),” “(b),” “(c),” “(d),” and “(e)” refer to Refs.<sup>20, 25–28</sup> (Reproduced from Ref. <sup>29</sup> with permission from the American Physical Society, Copyright 2020).

2D phosphorus allotropes have been constructed by assembling the ultrathin metastable phosphorus nanotubes (PNTs) into films with different stacking orientations.<sup>30</sup> First-principles calculations show that these allotropes possess remarkable stabilities due to the strong inter-tube van der Waals interactions. Two of the structures have non-centrosymmetric stacking and thus exhibit piezoelectric properties. The calculated piezoelectric coefficients for PNT(0,0.5) are  $d_{11} = -8.26 \text{ pm V}^{-1}$  and  $d_{12} = -0.13 \text{ pm V}^{-1}$ , and  $d_{11} = -7.57 \text{ pm V}^{-1}$  and  $d_{12} = 0.05 \text{ pm V}^{-1}$  for PNT(30,0.5).<sup>30</sup>

One of the challenges of working with phosphorene is that it readily oxidises. This is especially true for structures with less

than 4 layers. First principles calculations have been used to study the electronic structures and piezoelectricity of a series of 2D monolayer phosphorene oxides (POs).<sup>24</sup> Some of the monolayer PO materials have large in-plane and out-of-plane piezoelectric coefficients. For example, a  $d_{11}$  of  $54 \text{ pm V}^{-1}$  and  $d_{31}$  of  $-10 \text{ pm V}^{-1}$  for a  $P_4O_2$  structure with single-sided oxygen atoms and  $d_{26}$  of  $21 \text{ pm V}^{-1}$  for  $P_4O_2$  structures with double-sided oxygen atoms have been calculated (Figure 5a). In the stoichiometric  $P_4O_4$  configuration, each phosphorus atom adsorbs an oxygen atom on the surface, which dramatically changes the structural properties of the bare phosphorene and increases its ionic character. Similar work calculated a  $d_{11}$  of  $88.54 \text{ pm V}^{-1}$ .<sup>31</sup> An alternative ground state of PO proposed by Li *et al.*<sup>30</sup>, involving a twist-boat configuration of  $\theta$ -P with distorted surface oxidation (Pca21-PO), had a  $d_{12}$  of  $50.32 \text{ pm V}^{-1}$ . The authors showed that Pca21-PO was highly stable and energetically more favourable than the previously explored Pmn21-PO ground state.<sup>24, 31</sup> It is clear that the concentration and position of dangling oxygen atoms can significantly influence the piezoelectricity of monolayer POs (Figure 5, left). The calculated piezoelectric coefficient  $d_{11}$  of  $54 \text{ pm V}^{-1}$  in POs is much larger than those of some conventional 2D piezoelectric materials such as  $\text{MoS}_2$ , BN, and GaSe ( $d_{11} = 3.73 \text{ pm V}^{-1}$ ,<sup>14</sup>  $d_{11} = 0.60 \text{ pm V}^{-1}$ ,<sup>14</sup> and  $d_{11} = 2.30 \text{ pm V}^{-1}$ , respectively).<sup>23</sup> The fact that the PO is oxidised suggests that it could be quite stable and find many applications. However, simulation studies have shown that PO can become insulating at the highest oxidation levels of  $P_4O_8$  or  $P_4O_{10}$ , due to oxygen in the structure breaking the conjugation and localizing the conduction and valence bands.<sup>32</sup> This means utilizing PO for devices will require control over the degree of oxidation, but will nonetheless be useful due to increased stability. Adsorption of other atoms on the 2D crystals may also lead to enhanced properties and this represents an important avenue for future investigation.

Like graphene, the effects of various adatoms on the piezoelectric coefficients of phosphorene have been explored using density functional theory (DFT) calculations. All metallic elements in the top three rows of the periodic table were used in turn as adatoms, with a broad range of concentrations from  $P_{48}X_1$  to  $P_4X_2$ . Amongst the wide range of values obtained, Li-doped black P ( $P_4\text{Li}_2$ ) had a  $d_{31}$  value of  $6.28 \text{ pm V}^{-1}$ , at least three times larger than that for any other 2D piezoelectric material (Figure 5b). A second calculation using a more complicated DFT-Tkatchenko-Scheffler (TS) approach yielded significantly smaller  $d_{31}$  value of  $2.5 \text{ pm V}^{-1}$  for  $P_4\text{Li}_2$ . The results show that there is no clear relationship  $d_{31}$  calculated using the PBE function and the more ‘accurate’ TS functional (Figure 5b), highlighting a central problem of DFT, where there is no available systematic approach to improve the result. This highlights the unresolved computational challenges in accurately predicting piezoelectric coefficients, particularly for van der Waals materials.<sup>29, 33</sup>

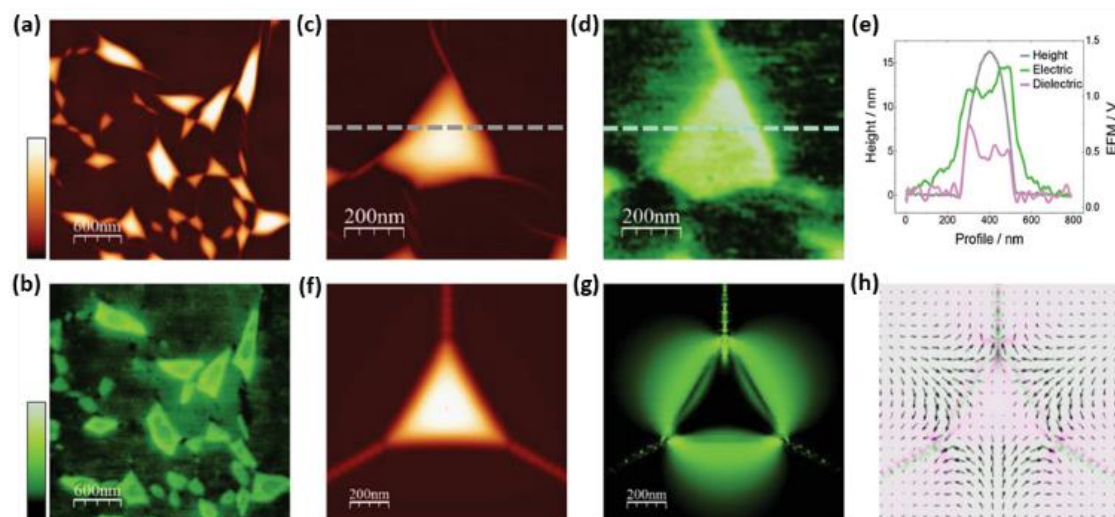


**Figure 6.** Bubble formation in h-BN crystals. (a) Topography of h-BN with bubbles and creases; (b) electrostatic force microscopy (EFM) electric image of the same region as (a); (c) topography and (d) EFM electric images of a triangular shaped bubble; (e) height, electric, and dielectric profiles along the lines in (c) and (d); (f) simulated topography image of a triangular bubble in monolayer h-BN; (g) calculated electric-field energy density of (f); and (h) vector field polarization and (coloured) charge distribution. Colour scales (from dark to bright): topography (both experimental and simulated) 20 nm; EFM 1.5 V; electric field energy density  $1.5 \mu\text{V} \text{ \AA}^{-2}$ ; charge distribution  $-6 \times 10^{12}$  (green) to  $6 \times 10^{12}$  (pink)  $\text{e}^- \text{cm}^{-2}$  (Reproduced from Ref. <sup>34</sup> with permission via CC-BY licence from Wiley & Sons, Copyright 2020)

Normally piezoelectricity is limited in multilayer 2D crystals because of the opposing orientations of adjacent atomic layers. This effect is minimal in black phosphorous lattices due to their spring-shaped space structure.

The structure results in the charges within the top and bottom half-layers aligning in antiparallel directions as strain is applied along the armchair in-plane direction.<sup>22, 35</sup> This effect occurs even in multilayer BP, although the adjacent layers may reduce the measurable piezoelectric response. Ma *et al.*<sup>35</sup> have used this to advantage to confirm experimentally the existence of in-plane piezoelectricity for multilayer BP along the armchair direction. Current–voltage measurements demonstrated a piezo-tronic effect (modulation of semiconductor band structure by strain induced piezoelectricity)<sup>36</sup> in this orientation. Cyclic compression and release of BP flakes with an approximate thickness of 18 layers generated an intrinsic current as large as 4 pA under a compressive strain of 0.72%.<sup>36</sup>

### c. Antimonene

Recent success in the isolation and synthesis of highly stable and atomically thin antimonene has triggered great interest. Calculations have shown that the application of uniaxial strain along the zigzag and armchair directions generates direction-dependent trends in the electronic band structure, suggesting potential future use in nanoelectromechanical systems.<sup>37</sup> Additionally, some energetically stable allotropes of antimonene and arsenene have been predicted to possess very high lattice strain limits of up to 58% and 24% in the armchair and zigzag direction respectively, much higher than any other 2D crystal (e.g., graphene, MoS<sub>2</sub> or phosphorene).<sup>38</sup> Lu *et al.*<sup>39</sup> investigated the electronic structures of, and the biaxial strain effect in, antimonene-based van der Waals heterostructures using first principles calculations. They combined antimonene

(Sb) with semi-metallic graphene (G), semi-conducting arsenene (As) and insulating h-BN to generate three new 2D van der Waals heterostructures, namely, G/Sb, As/Sb and h-BN/Sb. With biaxial strain, continuously controllable band gaps from 0 eV to 1 eV were observed, corresponding to spectral ranges from near-infrared (NIR) to mid-infrared (MIR). These exceptionally large, stable, lattice strains, in conjunction with strain-tuneable and directional electronic properties suggest that antimonene may become a material of great interest for engineering piezoelectric properties in 2D crystal heterostructures. These heterostructures could have applications in infrared detectors, photoelectric, or microelectronics piezoelectric devices. Despite these recent successes, there are virtually no reports of piezoelectric outputs from antimonene to date, hence this exciting material is not discussed further here.

### d. Hexagonal boron nitride

Hexagonal boron nitride (h-BN) is an interesting case. In its monolayer form it has no center of symmetry and is thus expected to have a degree of piezoelectric properties.<sup>14, 40</sup> However, there is a paucity of experimental evidence for the piezoelectricity in h-BN. Recently, Ares *et al.*<sup>34</sup> calculated a piezoelectric coefficient of  $\gamma \approx 291 \text{ pC m}^{-1}$  for h-BN, mimicking data obtained by electrostatic force microscopy, and comparable to that of other (non 2D) piezoelectric ceramics including, zinc oxide (ZnO), aluminum nitride (AlN), and lead zirconate titanate ( $\text{Pb}[\text{Zr}_x\text{Ti}_{1-x}]\text{O}_3$ , PZT) ceramics.<sup>41, 42</sup> This was attributed to nanoscale strain being induced in the lattice by the applied electric field (Figure 6).

These findings, particularly the influence of strain on the piezoelectric coefficient, are of seminal importance to unlocking next generation piezoelectric devices based on 2D crystals.

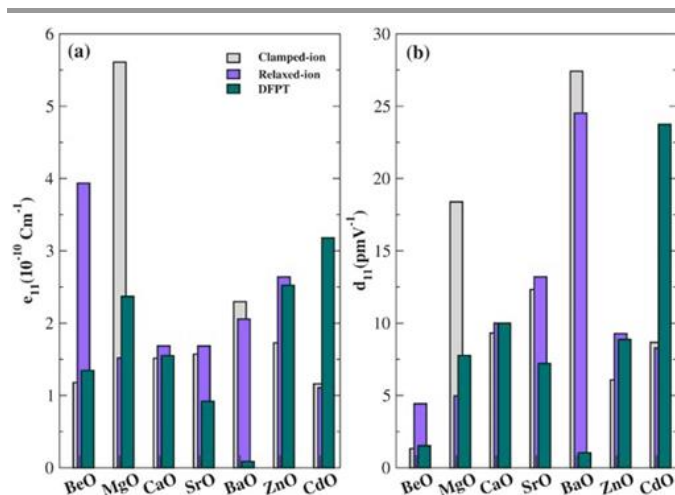


**Figure 7.** Calculated DFT (clamped-ion and relaxed-ion) and density functional perturbation theory values of in-plane (a) piezoelectric stress ( $e_{11}$ ) and (b) piezoelectric charge ( $d_{11}$ ) coefficients. (Adapted from Ref.<sup>43</sup> with permission from Wiley & Sons, Copyright 2016).

Nevertheless, further work is needed to realize the potential of h-BN for piezoelectric applications.

#### e. Metal Oxides

The emergence of liquid metal synthesis techniques has stimulated an upsurge in the production and customization of 2D metal oxide systems.<sup>44, 45</sup> 2D metal oxides display a variety of crystal structures. While PZT is the most commonly studied piezoelectric ceramic material in bulk, there are very few metal oxides in the 2D form that show significant out-of-plane piezoelectric effects.<sup>43</sup> One exception was reported recently by Ghasemian *et al.*<sup>46</sup>, using a liquid metal synthesized lead oxide (PbO). This orthorhombic 2D-PbO showed a  $d_{33}$  of 30.41  $\text{pm V}^{-1}$  and a  $d_{31}$  of 18.9  $\text{pm V}^{-1}$ , one of the highest reported for 2D crystals. While it remains significantly lower than that of the benchmark piezoelectric ceramic PZT, the work highlights the ability to produce environmentally friendlier, yet chemically similar, piezoelectric 2D crystals.

While minimal out-of-plane piezoelectric performance has been reported for metal oxides, Alyoruk<sup>43</sup> performed detailed simulations on 2D metal oxides to elucidate their in-plane strain and charge coefficients (Figure 7). These values ranged up to 25  $\text{pm V}^{-1}$ , showing the promise of 2D metal oxides for future piezoelectric applications.

#### f. Transition Metal Chalcogenides

Transition metal chalcogenides (TMCs) are one of the most thoroughly studied 2D piezoelectric materials. The piezoelectric properties result from a buckled, and asymmetric structure that has intrinsic in-plane and out-of-plane piezoelectricity.

Recently emerging monolayer group-IV monochalcogenides, including tin selenide (SnSe), tin sulphide (SnS), germanium selenide (GeSe), and germanium sulphide (GeS), have large predicted  $d_{11}$  coefficients (between 75  $\text{pm V}^{-1}$  and 250  $\text{pm V}^{-1}$ ).<sup>47</sup>

They are also predicted to be more resistant to oxidation in ambient air compared to phosphorene or arsenene, with approximately double the activation energy for dissociation/chemisorption of  $\text{O}_2$ .<sup>48</sup>

These predictions were recently validated by Khan *et al.*<sup>49</sup>, who demonstrated a high piezoelectric output in the 11 and 31 modes for liquid metal exfoliated SnS. Frustratingly, the authors did not report experimentally derived  $d_{11}$  and  $d_{31}$  coefficients, with only the calculated  $d_{11}$  (in-plane) coefficient of  $-144 \text{ pm V}^{-1}$  being provided.<sup>50</sup> However, the material they produced exhibited remarkable performance, with an output voltage of 150 mV at just 0.7% strain.<sup>49</sup> Further meticulous studies were performed to rule out triboelectric or flexoelectric contributions to this voltage, so this material represents one of the highest measured piezoelectric voltages for a monolayer.

While many different transition metal dichalcogenides and dioxides have been studied for piezoelectric properties, these studies have focused nearly exclusively on in-plane piezoelectric outputs.<sup>51</sup> This is due to the intrinsic symmetry of these triatomic-layer materials in the z-direction (and, unlike h-BN, these do have a defined center of symmetry).

#### g. Transition Metal Dichalcogenides

Transition metal dichalcogenides (TMDs, Figure 4e) have recently created huge research interest due to their typical layer-dependent electronic structure, absorbance in the visible range, and predictable chemistries useful for a very wide range of electronic and opto-electronic applications. TMDs have three main crystal phases, 2H, 1T, and 1T' (with variations including  $T_d$ ), with dramatically different properties. For instance, the thermodynamically stable phase for tungsten selenide ( $\text{WSe}_2$ ) is the semiconducting 2H phase, but it can be converted into the topologically insulating 1T' phase through rapid cooling, or by induced strain during synthesis.<sup>52-55</sup>

$\text{SnSe}_2$  should not exhibit intrinsic out-of-plane piezoelectricity, so the recent report of piezoelectric  $\text{SnSe}_2$  pressure sensors highlights the challenges in understanding and assessing the performance of 2D crystals as piezoelectric devices.<sup>56</sup> A paper substrate impregnated with monolayer  $\text{SnSe}_2$  exhibited exceptional performance as a pressure sensor (611% responsivity and sensitivity of 1.79  $\text{kPa}^{-1}$ ), attributed to the piezoresistive effect of  $\text{SnSe}_2$ .<sup>56</sup> However, there was no fundamental characterization of the piezoelectric output so it cannot be confirmed whether the change in resistance is driven by piezoelectricity of the  $\text{SnSe}_2$  (potentially arising from Se vacancies), or from friction (and hence triboelectricity)<sup>11</sup> between the  $\text{SnSe}_2$  and the paper substrate.

Similarly,  $\text{SnS}_2$  recently demonstrated an out-of-plane piezoelectric coefficient of approximately 2.2  $\text{pm V}^{-1}$ .<sup>57</sup> This  $d_{33}$  value was found to decrease with increasing  $\text{SnS}_2$  layer number, resulting in a 37% reduction as thickness increases from 4 nm to 9.2 nm.

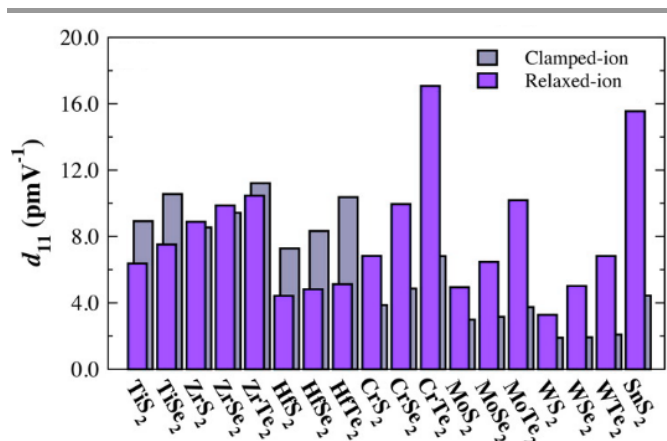


**Figure 8.** Calculated clamped and relaxed-ion piezoelectric strain ( $d_{11}$ ) coefficient for 2H transition metal dichalcogenides (Adapted from Ref. <sup>51</sup> with permission from the American Chemical Society, Copyright 2015).

Beyond these studies of Sn-based TMDs, few reports exist on out-of-plane piezoelectricity in pristine TMDs due to their centrosymmetric crystal structures. However, there are numerous papers detailing the in-plane piezoelectric output (Figure 8). These papers generally follow the rule that for a given transition metal system, the in-plane piezoelectric coefficient will increase with the atomic number of the chalcogen atom ( $S < Se < Te$ ). No clear trend is observed for the size or atomic number of the transition metal atom component. The dependence on the atomic number of the chalcogen atom is assumed to arise from increasing internal relaxation with higher atomic number chalcogens.<sup>51</sup> Furthermore, Te is the most easily polarized chalcogen due to its larger size, which generates increased lattice strain.<sup>51</sup> These calculations are performed assuming a 2H crystal structure,<sup>51</sup> yet many TMDs are thermodynamically stable in a centrosymmetric 1T structure. The approach remains valid as phase engineering for the control of electronic and optical properties is a key advantage of TMDs.<sup>58</sup> TMDs with versatile compositions and analogous crystal structures are a powerful tool for studying the effect of lattice strain, stacking, defects, and atomic size on piezoelectric properties moving forward.

#### h. Perovskites

Layered materials with unit cells thicker than three atomic layers have the advantage of possessing non-centrosymmetric crystal structures in thermodynamically stable phases.<sup>53</sup> These classes of materials show great promise for piezoelectric applications, however they are typically difficult to fabricate and handle.<sup>59</sup>

Perovskites have the general crystal formula of  $ABX_3$  (Figure 4a) and a massively diverse range of chemistries. Although they are heavily studied for solar applications, they are not often examined for piezoelectric properties.<sup>60</sup> Indeed, recent reports on exploiting potential piezoelectric outputs from 2D perovskites have still focused on using piezo-photo-tronic effects to enhance their device performance in solar cells.<sup>61,62</sup>

Ferroelectricity (and hence piezoelectricity) may be observed in traditional perovskite structures (such as  $PbTiO_3$  and  $BaTiO_3$ ) down to few unit cell thickness (broadly  $<3$  nm).<sup>63-66</sup> These discoveries have been enabled by rapid advances in the synthesis and isolation of thin perovskite layers.<sup>67</sup> One of the clearest examples is the work by You *et al.*<sup>68</sup>, that describes in-plane ferroelectric output from vdW barium lead chloride ( $Ba_2PbCl_4$ ) down to two layers at room temperature. One of the key challenges in developing perovskite-based ferroelectrics is the difficulty of fabricating homogenous perovskite layers (with no point defects/pinholes) less than 3 atomic layers thick.<sup>63,69</sup> Recent work by Nordlander *et al.*, has surpassed the previously hypothesized thickness limitation, demonstrating polarization in half-unit cell thick perovskites.<sup>70</sup> However, while the half-unit cell possesses the broken inversion symmetry required for the piezoelectric effect, exploiting these properties remains extremely challenging. In spite of this challenge, this is a significant advance and presents a unique opportunity for future 2D perovskite piezoelectric crystals.<sup>70</sup>

It should also be noted that comparing the piezoelectric properties of perovskites to other 2D crystals is challenging, as these materials nearly always have their ferroelectric properties reported. This does not lend itself to direct comparison with piezoelectric vectors in the 11, 31, or 33 directions. For this reason, a detailed examination of ferroelectric perovskites is not undertaken here, however an excellent review of this field is provided by Qi, Ruan, and Zeng.<sup>71</sup>

#### i. MXenes

As an emerging class of materials, MXenes are of great interest for a diverse range of applications because of their exceptional electronic, mechanical, and chemical properties. MXenes are a family of 2D inorganic compounds with the general formula of  $M_{n+1}X_nT_x$ , where M is a transition metal, X is carbon and/or nitrogen, and T is a functional group on the surface of the MXene (typically O, OH and F). Of specific interest for piezoelectric applications is their large out-of-plane electrostatic field,<sup>10</sup> and their versatile surface chemistry that enables (relatively) simple manipulation of their properties without compromising their electrical and mechanical properties.<sup>59</sup>

While electrostatic shielding applications have been widely reported for MXenes,<sup>72,73</sup> only a few papers report their piezoelectric properties.<sup>74</sup> Out-of-plane piezoelectricity in MXenes was reported by Tan *et al.*<sup>74</sup> They used oxygen functionalized MXenes with the general formula  $M_2CO_2$ . Their calculated piezoelectric  $d_{31}$  coefficients ranged between 0.40 pm V<sup>-1</sup> and 0.78 pm V<sup>-1</sup>. The authors claimed that the  $Sc_2CO_2$  monolayer had the largest out-of-plane  $d_{31}$  of all atomically thick 2D crystals studied. This may be exceeded and this work highlighted the considerable potential of MXenes as piezoelectric materials.

### j. Anti-MXenes

Recently, Gu *et al.*<sup>75</sup> reported the fabrication of a new class of 2D crystals, the anti-MXenes (Figure 9). These materials consist of two metal atoms and two X layers within a unit cell, forming a square shape when looking top down (e.g., cobalt boride (CoB) (Figure 9a), cobalt CoSi (Figure 9b), copper sulphide (CuS) (Figure 9c) etc). Crucially, these anti-MXenes have been predicted to be thermodynamically and mechanically stable.

This seminal report did not cover piezoelectric properties, however, their asymmetry in the z-direction suggests they may be intrinsically piezoelectric. Furthermore, the exposure of surface metal atoms is ideal for functionalization that can be used to further induce or enhance out-of-plane piezoelectric responses. Due to the paucity of publications on the intrinsic piezoelectric properties of anti-MXenes, they will not be discussed further. However, the potential for inducing piezoelectric effects makes these materials attractive for further study.

### k. Ternary Chalcogenides

The most well studied out-of-plane piezoelectric effects are in 2D crystals with the general formula  $M_2C_3$  (where M = metal, and C = chalcogen). Intrinsic asymmetry in the z-direction leads to ferroelectric behaviour, notably in  $\alpha$ - $In_2Se_3$  that has an R3m crystal symmetry.<sup>76</sup> Interestingly, the  $d_{33}$  of  $\alpha$ - $In_2Se_3$  is thickness dependant, reaching a constant value at thicknesses  $>50$  nm (Figure 10).<sup>77</sup> This thickness dependence arises from decreased substrate constraints on the piezoelectric response and has also been reported in other layered ferroelectric materials including PZT and  $CuInP_2S_6$ .<sup>78, 79</sup>

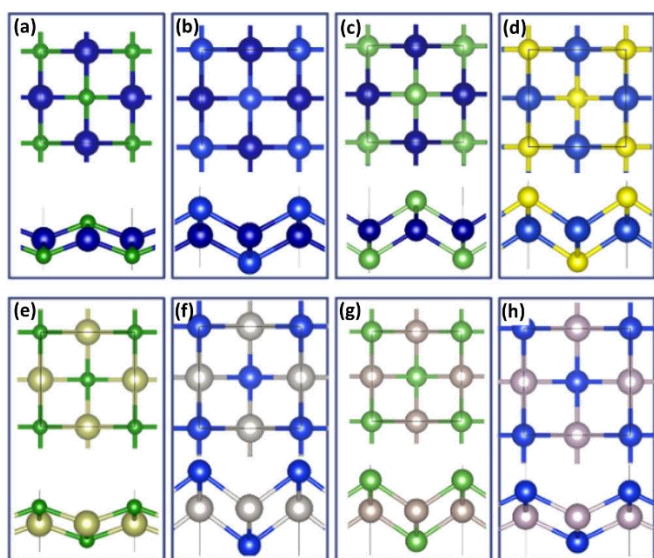


**Figure 9.** The structure of eight anti-MXenes: (a) CoB, (b) CoSi, (c) CrAs, (d) CuS, (e) IrB, (f) PtSi, (g) RuAs, and (h) TcSi. (Co = ●; B = ●; Si = ●; Cr = ●; As = ●; Cu = ●; S = ●; Ir = ●; Pt = ●; Ru = ●; and Tc = ●) (Reproduced from Ref. <sup>75</sup> with permission from the American Chemical Society, Copyright 2021)

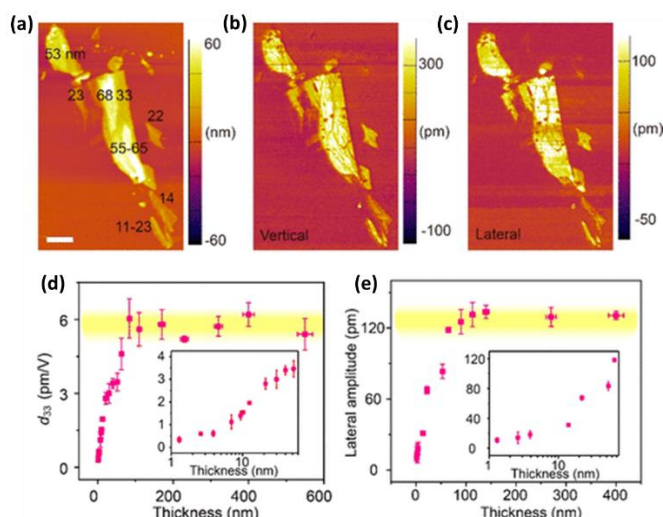


**Figure 10.** (a) Atomic force microscopy (AFM) (labels on image denote thickness); (b) vertical piezo-force microscopy (PFM); and (c) lateral PFM images for a  $>9L$  thick  $\alpha$ - $In_2Se_3$  sample (Scale bar:  $5 \mu m$ ); (d) Thickness dependence of the  $d_{33}$  piezoelectric coefficient for  $\alpha$ - $In_2Se_3$  (inset: enlarged  $d_{33}$  coefficient and thickness below  $60$  nm). The effective  $d_{33}$  piezoelectric coefficient for the monolayer  $\alpha$ - $In_2Se_3$  crystal is approximately  $0.3 \text{ pm V}^{-1}$ , and that for thick samples ( $>90$  nm) saturates at approximately  $5.6 \text{ pm V}^{-1}$ ; and (e) Lateral PFM amplitude (piezoresponse) as a function of  $\alpha$ - $In_2Se_3$  thickness (inset: enlarged lateral amplitude at less than  $60$  nm). It also presents a saturated trend when the thickness reaches  $\sim 90$  nm. The horizontal and vertical error bars represent the standard deviations of sample thickness and piezoelectric response. Note that the background noise has been deducted for all the presented data here. (Reproduced from Ref. <sup>77</sup> with permission from the American Chemical Society, Copyright 2018)

Intriguingly, while  $Bi_2Se_3$  and  $Bi_2Te_3$  have equivalent crystal structures to that of  $In_2Se_3$ , the bismuth-based materials have not yet been investigated as piezoelectric materials. However, hybrid monolayers of  $BiInSe_3$ ,  $BiInTe_3$ ,  $SbInSe_3$ , and  $SbInTe_3$  have been shown theoretically to possess exceptional in-plane piezoelectric coefficients of up to  $362 \text{ pm V}^{-1}$ .<sup>80</sup> This value would be comparable to the out-of-plane piezoelectric coefficients of the leading ceramic material PZT, however experimental synthesis and validation of these predictions are challenging. Summary of monolayer 2D crystals The prior sections have provided an overview of piezoelectric properties in a selection of the more common 2D monolayers. It is clear that only a few 2D monolayer materials exhibit strong out-of-plane polarization and/or piezoelectric effects, with a notable exception being  $In_2Se_3$ . This presents a quandary when designing devices that exploit the piezoelectric effect. Thus, the following section will discuss approaches to engineer large out-of-plane piezoelectric responses.

## 3. Engineering piezoelectricity in 2D crystals

### a. Stacking 2D Heterostructures – Unlocking Unique Piezoelectric Outputs

#### Stacking Dissimilar 2D crystals

The development of z-direction piezoelectricity in 2D crystals with diverse chemical properties requires the assembly of van der Waals heterostructures. These structures can be further manipulated by phase-engineering processes to unlock unique

symmetries and electronic properties. However, when assembling heterostructures from dissimilar 2D crystals, the mechanism of stacking and the interface between the materials are crucial to understand.<sup>58</sup> A major limitation is that common solution phase heterostructuring approaches leave unwanted species between layers and often cause non-conformal restacking (Figure 4f).<sup>81</sup> While such systems are still useful for electronic and charge transport applications, they do not have a coherent heterostructure unit-cell that is required for fundamental properties such as piezoelectricity. However, deposition systems such as chemical vapor deposition (CVD)<sup>82</sup> and mechanical transfer enable the fabrication of epitaxial and coherent interfaces, where the structure is connected into a single unit cell (Figure 4f).

Piezoelectricity in heterostructures from dissimilar 2D crystals was first predicted by Mohanta et al. for GaN/boron monophosphide crystals.<sup>83</sup> These heterostructures were predicted to have a  $d_{33}$  of up to 40 pm V<sup>-1</sup>. Subsequent predictions have shown that 2D crystal heterostructures with large out-of-plane piezoelectricity can be produced using constituent 2D crystals that only possess in-plane piezoelectricity.<sup>84, 85</sup>

Several recent studies have subsequently reported synergistically enhanced piezoelectric responses greater than the sum of the individual heterostructure components. Yuan et al.<sup>86</sup> have fabricated In<sub>2</sub>Se<sub>3</sub>/molybdenum sulfide (MoS<sub>2</sub>) heterostructures from mechanical exfoliation, demonstrating an increase in the  $d_{33}$  from 7.5 pm V<sup>-1</sup> for In<sub>2</sub>Se<sub>3</sub> to 17.5 pm V<sup>-1</sup> for the In<sub>2</sub>Se<sub>3</sub>/MoS<sub>2</sub> heterostructure.<sup>86</sup> This is particularly interesting as MoS<sub>2</sub> does not have any intrinsic z-direction piezoelectric output, as described in Section 2g. This exemplifies the potential of heterostructure formation towards introducing piezoelectric properties into non-piezoelectric materials. The

role of electronic band offset of the heterostructure constituents is clearly demonstrated to result in a large interfacial dipole that complements the polarization of the underlying In<sub>2</sub>Se<sub>3</sub> sheet. A similar heterostructure of In<sub>2</sub>Se<sub>3</sub>/WS<sub>2</sub> was shown to have a  $d_{33}$  of 10.7 pm V<sup>-1</sup>. The key difference between In<sub>2</sub>Se<sub>3</sub>/MoS<sub>2</sub> and In<sub>2</sub>Se<sub>3</sub>/WS<sub>2</sub> heterostructures was their relative band offsets of 0.8 eV and 0.6 eV, respectively, leading to the significantly improved performance from the MoS<sub>2</sub> based heterostructure.

The structural properties of black phosphorus (Black P)/MoS<sub>2</sub> van der Waals heterostructures have been investigated using first principles calculations.<sup>87</sup> This work showed that an applied compressive strain has minimal effect on the optical properties in the X and Y directions but a remarkable effect on the three optical parameters in the perpendicular direction. This suggests that good piezoelectric effects may be realized in BlackP/MoS<sub>2</sub> heterostructures. Blue phosphorene, an allotrope of the BlackP, was first produced experimentally on an Au(111) substrate in 2016.<sup>88</sup> The blue phosphorene was found to have no intrinsic piezoelectric properties, but some heterobilayers, predicted by computational approaches, may exhibit them. For example, the out-of-plane piezoelectric response of a selenium molybdenum sulfide (SeMoS)/BlueP was predicted to be approximately 3x larger than the Janus SeMoS monolayer alone.<sup>89</sup>

Jang et al.<sup>61</sup> have fabricated, or 'dimensionally engineered', a 2D/3D perovskite heterostructure. They deposited a thin 2D layer (<25 nm) of FAPbI<sub>3</sub> perovskite on an 800 nm 3D perovskite crystal. This 2D/3D heterostructure exhibited a synergistic increase in  $d_{33}$  from 2.77 pm V<sup>-1</sup> and 3.73 pm V<sup>-1</sup> for the 2D and 3D constituents, respectively, to 4.33 pm V<sup>-1</sup> for the 2D/3D heterostructure. This approach is exploited for piezophototronic effects that boost photocurrent output of solar cells.

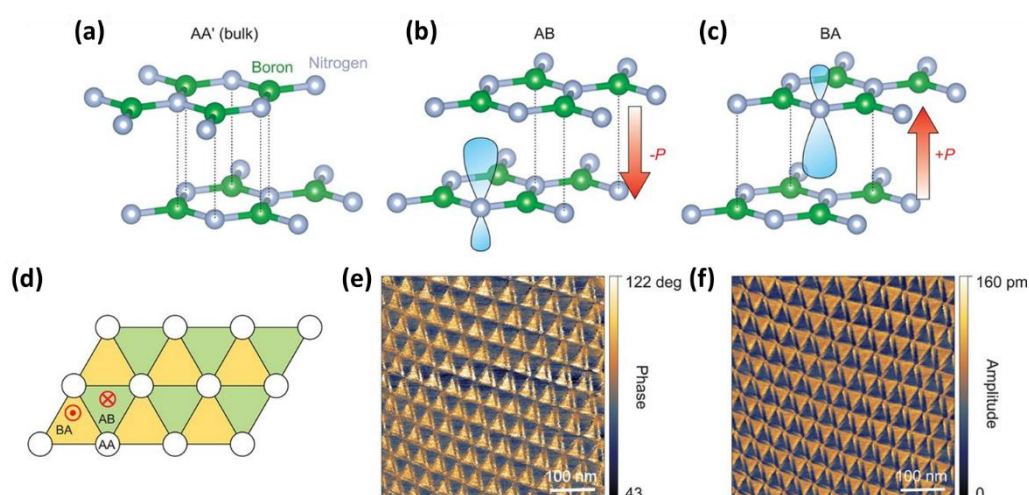


**Figure 11.** Illustration of the atomic arrangement for (a) AA' stacking in the bulk form of hBN. Nitrogen and boron atoms are shown in silver and green, respectively. (b and c) Illustration of the atomic arrangement for AB and BA stacking. The vertical alignment of nitrogen and boron atoms distorts the 2p, orbital of nitrogen (light blue), creating an out-of-plane electric dipole. (d) Illustration of a small angle twisted bilayer BN after the atomic reconstruction. The reconstruction creates relatively large AB (green) and BA (yellow) domains, with small AA regions (white) and domain walls in between (black). The red circled dot and red circled X represent up and down polarization, respectively. (e and f) Vertical PFM phase and amplitude images of twisted bilayer BN. Scale bars are 100 nm. (Reproduced from Ref. <sup>90</sup> with permission from the AAAS, Copyright 2021)

### Stacking Similar 2D crystals (Twist Angle/Stacking Order)

While stacking of dissimilar materials should lead to emergent out-of-plane piezoelectric properties, achieving the same result from a bilayer of a single 2D crystal will not produce any change in the piezoelectric tensor. However, simply altering the stacking order and/or twist angle of a bilayer stack has recently been reported to induce a strong out-of-plane piezoelectric response. This breakthrough was reported simultaneously by Yasuda *et al.*<sup>90</sup>, Woods *et al.*<sup>91</sup> and Vizner Stern *et al.*<sup>92</sup>, using bilayer h-BN.

These teams independently reported that by identifying<sup>91</sup> or inducing<sup>90</sup> a shift from the anti-parallel stacking sequence, AA', of bulk h-BN (Figure 11a) to a parallel AB or BA stacking sequence (Figure 11b, c), out-of-plane polarization is achieved. Yasuda *et al.*<sup>90</sup> generated this shift in a parallel stacking sequence by forcing a small twist angle between the layers, which created alternating domains of 'up' polarization (BA, yellow, Figure 11d) and 'down' polarization (AB, green, Figure 11d). Probing the samples by piezoforce microscopy (PFM) clearly demonstrated the emergence of domains with these alternating polarizations (Figure 11 e and f). Vizner Stern *et al.*<sup>92</sup> used a similar approach and noted the polarization in the h-BN bilayers was flipped by domain wall-sliding.

Beyond h-BN, out-of-plane piezoelectric effects were recently reported by Zheng *et al.*<sup>93</sup> in graphene bilayers using a similar dry transfer and twisting technique. Note that the emergence of out-of-plane polarization was studied at a reduced temperature of 4 K, compared to room temperature for the aforementioned h-BN samples. Nonetheless, these results generated a paradigm shift that will enable future design of piezo- and ferro-electric 2D devices from non-polar materials. Critically, for these bilayers of similar 2D crystals, techniques to induce out-of-plane polarization are difficult and not scalable. Thus, similar 2D heterostructures are ideal for probing fundamental properties, and exploring the physics within but only at the lab scale. For exploitation of the out-of-plane piezoelectric effect for real commercial devices, dissimilar 2D heterostructures (Figure 4f), where stacking order can be largely discounted, appear more promising.

Recent work by McGilly *et al.*<sup>94</sup> and Li *et al.*<sup>95</sup> have produced Moiré superlattices from twisted graphene bilayers. Interestingly, an alternative mechanical-to-electrical conversion mechanism, the flexoelectric effect, is observed in these non-piezoelectric crystals. These works serve to highlight a key challenge in experiment measurement and quantification of the piezoelectric effect, the deconvolution of piezoelectric, triboelectric, and flexoelectric contributions.<sup>11, 96</sup>

Clearly, heterostructures are an emerging, promising approach to tuneable properties and device performance in 2D crystals. However, with continued development of experimental techniques for reproducible heterostructure fabrication, the flexibility of combining any given van der Waals 2D crystals will

lead to unprecedented piezoelectric device performance from these 2D constructs.

### b. Manipulating Chemistries

The conventional way to change the chemical and/or physical properties of a given material is through structural modification. We have tangentially discussed this above, comparing In<sub>2</sub>Se<sub>3</sub> to BiInSe<sub>3</sub> type systems, however the approach is much more general and, importantly, can induce piezoelectric response in non-polar materials.

### Defects

The introduction of defects into the surface of a 2D crystal is an obvious way to induce a *local* asymmetry and hence out-of-plane piezoelectric response. The primary challenge here is to translate this local breaking of symmetry into a macroscale device performance. The best example reported in literature to date is that of Kang *et al.*,<sup>97</sup> using molybdenum telluride (MoTe<sub>2</sub>). They showed that generation of Te vacancies in MoTe<sub>2</sub> by thermal annealing dramatically increased the  $d_{33}$  from  $\sim 0.4$  pm V<sup>-1</sup> to  $\sim 2.4$  pm V<sup>-1</sup> (Figure 12 a-c). This corresponded to a decrease in the Te:Mo stoichiometry from 2.0964 to 2.0023, respectively. As the net value of Te:Mo was still greater than the stoichiometric ratio of 2.0000, it is hard to draw conclusions about the specific defect density required to optimize the piezoelectric output. This approach to inducing out-of-plane piezoelectricity will require further fundamental studies.

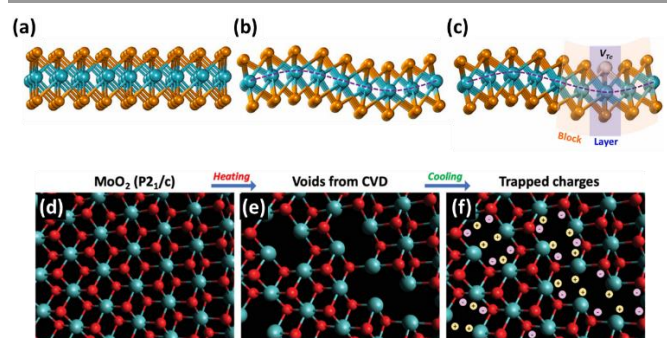


**Figure 12.** Defects in different 2D crystals leading to enhanced piezoelectric output; a-c) in MoTe<sub>2</sub>; a) flat crystal structure; b) corrugated crystal structure; and c) corrugated crystal structure with Te defects (a-c, Reproduced from Ref. <sup>97</sup> with permission from Elsevier, Copyright 2018); d-f) in MoO<sub>2</sub>; d) pristine MoO<sub>2</sub>; e) voids formed during chemical vapour deposition growth; and f) charge trapping leading to ferroelectric formation during cooling from synthesis. (Reproduced from Ref. <sup>99</sup> with permission from Wiley & Sons, Copyright 2020.)

Recent work by Choi *et al.*<sup>98</sup> has highlighted different processing routes for exploiting the piezoelectric effect induced by defects on MoS<sub>2</sub>. Here, polycrystalline MoS<sub>2</sub> monolayers were produced by Mo sputtering followed by sulfurization via CVD. The samples were then exposed to a high temperature (350 °C to 450 °C) annealing process in the presence of toluene. This so called thermal-solvent annealing process led to sulfur (S)-vacancy formation. These S-vacancies were shown to lead to a suppression in electron density within the annealed MoS<sub>2</sub>, and a subsequent hole-rich system.

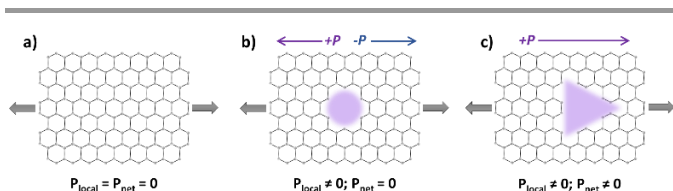


**Figure 13.** Schematic representation of the effect of pore geometry (represented by the shaded area) on the polarisation ( $P$ ) in a non-piezoelectric crystal; a) a non-porous, non-piezoelectric, shows no piezoelectric response under strain (directionally represented by dark arrows); b) the same crystal with an approximately circular pore demonstrating a non-zero local polarisation, not no overall net polarisation and thus no measurable piezoelectric response; and c) with a non-centrosymmetric (approximately) triangular pore, both local and net polarisations are non-zero, thus the material will exhibit apparent piezoelectricity. (Adapted from Ref. <sup>13</sup> with permission from Springer Nature, Copyright 2014.)

Coupled to this effect, was a variation in the atomic bonding length within the highly defected MoS<sub>2</sub> leading to broken inversion symmetry. Choi *et al.*<sup>98</sup> showed an out-of-plane piezoelectric (measured in the 33 mode) current and voltage of  $\pm 20$  pA and  $\pm 700$  mV, respectively, for the highly defected sample, approximately 20 times higher than pristine MoS<sub>2</sub>.

Alternatively, enhancement of piezoelectric output by passivating defects has been described by Han *et al.*<sup>100</sup> The authors passivated native S vacancies in MoS<sub>2</sub> monolayers, from a S:Mo ratio of approximately 1.8:1 to 2:1. This passivation led to strained nanosheets that generated a piezoelectric current of approximately 100 pA, three times higher than the unpassivated, defected MoS<sub>2</sub>. The authors postulated that this was due to the electron trapping nature of S-vacancies in MoS<sub>2</sub> limiting dipole deformation during straining, decreasing the free charge carrier concentration, and subsequently the piezoelectric output.<sup>100</sup> However, as is often the case in piezoelectric literature, the fundamental piezoelectric coefficients were not measured so it is difficult to draw concrete conclusions.

The results of Han *et al.*<sup>100</sup> are of particular interest as they conflict with a recent report of induced piezoelectricity in MoO<sub>2</sub> using charge trapping electrets by Apte *et al.*<sup>99</sup> Here, the authors showed that the centrosymmetric P2<sub>1</sub>/c MoO<sub>2</sub> did not exhibit intrinsic piezoelectricity. However, CVD treatment on the MoO<sub>2</sub> nanosheets (leading to void formation) resulted in significant piezoelectricity, with a  $d_{33}$  of between 0.072 pm V<sup>-1</sup> and 0.560 pm V<sup>-1</sup> (Figure 12d-f). The appearance of this piezoelectric output correlated with ‘bulk’ voids formed within the 2D sheets, resulting in charge trapping within the structure. These charge traps acted as ferroelectrets, inducing a piezoelectric response in out-of-plane deformation.<sup>99</sup>

Although graphitic carbon nitride (g-C<sub>3</sub>N<sub>4</sub>) is not discussed extensively in this review, Zelisko *et al.*<sup>13</sup> have provided an in-depth study on the effect of pore (or defect) geometry on the polarization of 2D crystals. They demonstrated that symmetrical pores lead to local polarization and no net piezoelectric output, while asymmetric pores lead to observed piezoelectricity (Figure 13).<sup>13</sup> These observations could form

the basis for bespoke introduction of pores in 2D crystals to modulate piezoelectric effects.

### Elemental Substitution

Elemental substitution, and the intentional formation of Janus type crystal structures, is one of the most promising approaches to induce out-of-plane piezoelectricity in 2D crystals. A good example is the group of Janus transition metal dichalcogenides, where sulfur can be selectively substituted for either Se or Te atoms on one basal plane surface. This substitution results in three key changes in the crystal structure; 1) a loss of symmetry across the z-direction; 2) an altered electron density leading to dipole formation in the z-direction; and 3) significant lattice strain to accommodate the size difference of the atoms on opposing layers.

Such a structure was first predicted theoretically by Cheng *et al.*<sup>101</sup> in 2013 for the family of MX<sub>2</sub> materials (where M = W or Mo, and X, Y = S, Se or Te). In 2017, these Janus crystals were experimentally reported by Lu *et al.*,<sup>102</sup> Zhang *et al.*,<sup>103</sup> and Dong, Lou, and Shenoy<sup>104</sup> who notably produced MoSTe, which showed a  $d_{33}$  up to 13.5 pm V<sup>-1</sup>. A comparison with other Janus structures showed that the magnitude of  $d_{33}$  correlates with the difference in atomic sizes of each chalcogen atom (thus MoSTe and tungsten sulfide telleride (WSTe) had the highest  $d_{33}$ ) (Figure 14a,b). Interestingly, the effect of stacking sequence was also investigated. In vertically asymmetric monolayers, the antiparallel stacking sequence (Figure 14 c) had a  $d_{33}$  more than twice that of a parallel stacking sequence (e.g., 13.5 pm V<sup>-1</sup> compared to 5.7 pm V<sup>-1</sup> for MoSTe).<sup>104</sup> This was consistent with the findings of Yasuda *et al.*<sup>90</sup> and Woods *et al.*<sup>91</sup> for hBN bilayers.

Subsequently, the field of piezoelectric Janus 2D crystals has continued to grow, with calculated structures including Ga<sub>2</sub>SSe, Ga<sub>2</sub>STe, Ga<sub>2</sub>SeTe, In<sub>2</sub>SSe, In<sub>2</sub>STe, In<sub>2</sub>SeTe, GaInS<sub>2</sub>, GaInSe<sub>2</sub>, GaInTe<sub>2</sub>,<sup>28</sup> Sb<sub>2</sub>Se<sub>2</sub>Te, Sb<sub>2</sub>Te<sub>2</sub>Se, SbAsSe<sub>2</sub>Te,<sup>105</sup> Te<sub>2</sub>Se,<sup>106</sup> SnSSe, GeSSe,<sup>107</sup> PtSSe, PtSTe, PtSeTe,<sup>108</sup> SbTeI, BiTeI,<sup>109</sup> and a family of MX<sub>2</sub>Y materials (M = Ti, Zr, or Hf, and X ≠ S, Se).<sup>110</sup> In each case, the  $d_{33}$  coefficient is calculated to be higher for the Janus 2D crystal compared to non-Janus analogues.

The chemical diversity of these computationally modelled structures suggests that, regardless of the constituent elements of a 2D crystal, producing a Janus structure will directly lead to the presence of a comparably large out-of-plane piezoelectric effect. Understanding this, the question becomes which constituent elements are the most appropriate to exploit. Critically there remain very few experimentally synthesised Janus 2D crystals, and approaches for atomically precise synthesis of more complex Janus crystals (beyond MX<sub>2</sub>) remain distant. Thus, significant focus should be directed to developing experimental methods to validate and support theoretical findings of Janus structures.

Recent works using computational approaches, led by Abir De Sarkar, have reported that applied strains may induce ultra-

high, colossal, or gigantic out-of-plane piezoelectricity to Janus 2D crystals.<sup>107, 110, 111</sup> These results, obtained using DFT, suggest that Janus MX<sub>2</sub> structures have chemical bonds more ionic than those in MX<sub>2</sub> crystals (wherein the bonds are predominantly covalent).<sup>111</sup> The increased ionic contribution to MX<sub>2</sub> bonds is suggested to lead to a lower electron deformation potential (and consequently a greater polarization). This lower deformation potential thus enables small in-plane strains to induce a dramatic change in dipole moment, and as a result the piezoelectric output. When extrapolated to other Janus monolayer structures, the effect of the change in bond nature is consistent with a calculated increase in electron and hole mobility, and enhanced piezoelectric effect under strain.<sup>107, 110</sup> The largest calculated  $d_{33}$  of 984 pm V<sup>-1</sup> was predicted to occur at 6% vertical compressive strain for a bilayer of TiSe<sub>2</sub>S (with the bilayer itself presenting a  $d_{33}$  of 541.29 pm V<sup>-1</sup>).<sup>110</sup> While the chemical stability of titanium chalcogenide structures is poor, due to oxidation to TiO<sub>x</sub>,<sup>112-114</sup> this work provides a strong proof-of-concept for using Janus 2D crystals to engineer the next generation piezoelectric 2D crystals.

These calculations provide a target and impetus for experimental replication. There is a challenge in achieving appropriate strains in experimental 2D crystals, with delamination, dislocation formation, and fracture/buckling acting as possible (albeit undesirable) strain relief mechanisms. However, recent work by Li et al.,<sup>115</sup> has reported tensile strain in WS<sub>2</sub> monolayers of up to 5.68% (attained by the radius of bending of 2D crystal monolayers encapsulated in a polymer) which is approaching the 6% strain used for the computed piezoelectric enhancements.<sup>110</sup> However, this is in-plane strain rather than compressive strain. Further work is needed to validate if strains approaching 6% can be experimentally realised for other 2D crystals (both in-plane and/or compressive), or if these predicted piezoelectric enhancements are observed at significantly lower strains. If these calculations are able to be reproduced experimentally, these atomically thin Janus 2D crystals would demonstrate record mechanical-to-electrical conversion efficiency.

Although the elemental substitution approach requires careful chemical control, it shows great potential as it allows the formation of out-of-plane dipoles with specific magnitudes and directions. Deconvoluting the specific role of elemental substitution and lattice strain is quite challenging, as switching specific surface atoms will automatically induce a strain on the other atoms within the unit cells. Therefore calculations, predictions, and interpretations must consider these strain effects in addition to changes in electronegativity (or charge localization) within the crystal structure.

In addition, it is important to take extreme care in the analysis and the simulation conditions for calculations involving variations in chemistry, induced strain and asymmetry. Such conditions can result in an asymmetric application of strain (i.e., strain gradient), consequently manifested as the combination of the piezoelectric and flexoelectric effect.<sup>116, 117</sup> The latter is

inherently difficult to discern, although the contribution of flexoelectricity can be minimised by confirming the absence of an inhomogeneous strain field parallel to the direction of polarisation following the simulations.<sup>118, 119</sup>

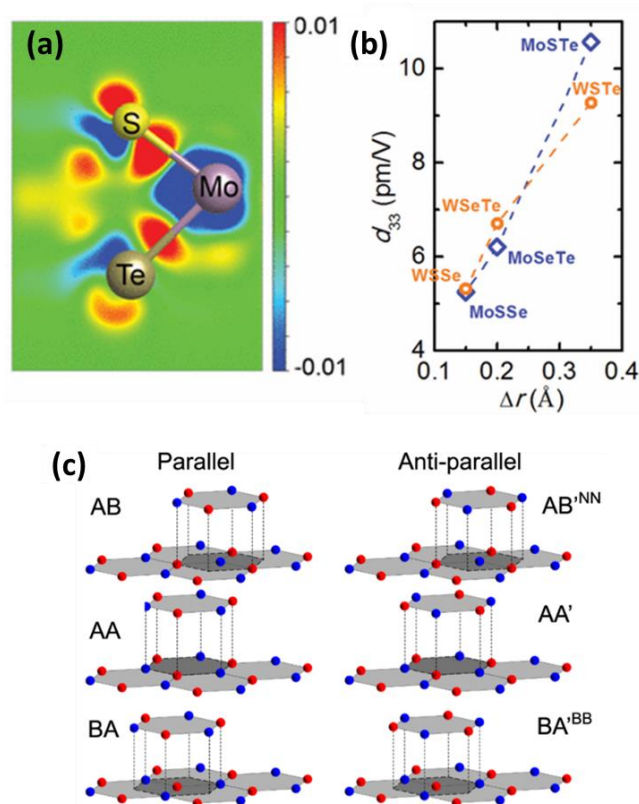


**Figure 14.** Janus transition metal dichalcogenides; a) charge density (units  $e/\text{Bohr}^3$ ) of MoSTe; b) comparison of  $d_{33}$  coefficient with differences in atomic radii of the chalcogen atoms; (a and b, Reproduced from Ref. 104 with permission from the American Chemical Society, Copyright 2017) and c) parallel (top) and antiparallel (bottom) stacking sequences for 2D crystals. (c, Reproduced from Ref. 91 with permission via CC-BY 4.0 licence from Springer Nature, Copyright 2021.)

The intrinsic and engineered piezoelectric outputs from selected 2D crystals are summarized in Table 1. From this data, the best piezoelectric 2D crystals are PbO, heterostructures with ferroelectric materials (In<sub>2</sub>Se<sub>3</sub>/WS<sub>2</sub> or In<sub>2</sub>Se<sub>3</sub>/MoS<sub>2</sub>), and Janus transition metal dichalcogenides. However, accurate and reproducible characterization and comparison remains challenging, with substantial ongoing debates around the best way to accurately measure piezoelectric properties *via* PFM on the nanoscale. Notably, a considerable number of studies in the area tend to use multiple different piezoelectric coefficients interchangeably, resulting in a lack of comparable data.

For example, the use of the piezoelectric stress coefficient in C m<sup>-1</sup> has been commonly observed, which arises by exchanging the value for the polarization in place of the displacement field; however, this is a value that cannot be confirmed experimentally by using Equation 3a. Nonetheless, the development of robust methods for engineering piezoelectric responses in non-polar crystals using heterostructures, and

defect engineering and elemental substitution will accelerate future design of piezoelectric 2D systems with bespoke properties. A major challenge is the breadth of potential chemistries and materials that can be combined or studied (the chemical space problem common to many areas of small molecule chemistry and materials science). To put this data into

perspective, the following section will review the use of machine learning to predict 2D heterostructure properties. With such a large amount of 2D crystals, the predictions enabled by machine learning is critical to designing materials with optimal piezoelectric outputs.

**Table 1.** Selected reporting of piezoelectric coefficients of 2D crystals.

2D crystal	Piezoelectric Coefficient	Comments	Reference
Graphene	$d_{33} = 37 \text{ nC N}^{-1}$	2D Band piezoelectric effect / strain engineering	19
MoTe <sub>2</sub>	$d_{33} = 0.4 \text{ pm V}^{-1}$	Up to $2.4 \text{ pm V}^{-1}$ locally in strained areas	97
SnS <sub>2</sub>	$d_{33} = 2.2 \text{ pm V}^{-1}$		57
In <sub>2</sub> Se <sub>3</sub>	$d_{33} = 0.34 \text{ to } 7.60 \text{ pm V}^{-1}$	Increases $d_{33}$ with increasing thickness	77, 86
PbO	$d_{33} = 30.41 \text{ pm V}^{-1}$	Liquid Metal Exfoliated	46
Sc <sub>2</sub> CO <sub>2</sub>	$d_{31} = 0.78 \text{ pm V}^{-1}$	Calculated via DFT, cantilever device showed piezoelectric output	74
Y <sub>2</sub> CO <sub>2</sub>	$d_{31} = 0.40 \text{ pm V}^{-1}$	Calculated via DFT, cantilever device showed piezoelectric output	74
La <sub>2</sub> CO <sub>2</sub>	$d_{31} = 0.65 \text{ pm V}^{-1}$	Calculated via DFT, cantilever device showed piezoelectric output	74
F, Li doped graphene	$d_{31} = 0.3 \text{ pm V}^{-1}$	Charge transfer to adatoms from graphene	20
MoTe <sub>2-x</sub>	$d_{33} = 2.4 \text{ pm V}^{-1}$	Defects induced via thermal annealing	97
Defected MoO <sub>2</sub>	$d_{33} = 0.072 \text{ to } 0.560 \text{ pm V}^{-1}$	Electret formation during synthesis, not intrinsic	99
In <sub>2</sub> Se <sub>3</sub> /MoS <sub>2</sub>	$d_{33} = 17.5 \text{ pm V}^{-1}$	Mechanically exfoliated samples	86
In <sub>2</sub> Se <sub>3</sub> /WS <sub>2</sub>	$d_{33} = 10.7 \text{ pm V}^{-1}$	Mechanically exfoliated samples	86
2D/3D FAPbI <sub>3</sub> (perovskite)	$d_{33} = 2.77 \text{ pm V}^{-1}$	Heterostructured embedded in TiO <sub>2</sub> /Spiro-OMeTAD	61
MoSTe	$d_{33} = 5.7 \text{ to } 13.5 \text{ pm V}^{-1}$		104
MoSeTe	$d_{33} = 6.217 \text{ pm V}^{-1}$		104
MoSSe	$d_{33} = 5.248 \text{ pm V}^{-1}$		104
WSSe	$d_{33} = 5.319 \text{ pm V}^{-1}$		104
WSeTe	$d_{33} = 6.710 \text{ pm V}^{-1}$		104
WSTe	$d_{33} = 9.279 \text{ pm V}^{-1}$		104
MoSeTe/WSTe	$d_{33} = 5.461 \text{ to } 13.91 \text{ pm V}^{-1}$	Stacking order dependant, calculated from DFT	120
ZrSe <sub>2</sub> S	$d_{33} = 68.72 \text{ pm V}^{-1}$	Calculated from DFT	110
Te <sub>2</sub> Se	$d_{33} = -89.338 \text{ pm V}^{-1}$	Calculated from DFT	106
TiSe <sub>2</sub> S	$d_{33} = 541.29 \text{ pm V}^{-1}$	Bilayer, stacking order dependant, calculated from DFT	110

\* 2D Crystals Defected/Doped Crystals 2D Heterostructures Janus 2D Crystals

#### 4. Machine Learning for 2D Heterostructure Properties

Following the first exfoliation of graphene in 2004, extensive research into the properties and applications of 2D crystals has led to the development of new types of electronic and optoelectronic devices.<sup>121</sup> As the research evolved, an entire new class of 2D crystals emerged that have been the focus of intense experimental and novel computational studies. The synergy between experiment and modelling has played a significant part in new material discovery and characterization. Multiple databases of novel 2D crystals have been compiled using experimental and computational methods to establish structure and function. These include the Inorganic Crystal Structure Database (ICSD), the superconducting critical temperatures (SuperCon), the Open Quantum Materials Database (OQMD), the Cambridge Structural Database, the

Harvard Clean Energy Project (HCEP), the Materials Project (MP), the Materials Commons, and the Materials Data Facility.<sup>122-128</sup>

However, van der Waals structures formed by combining 2D monolayers are sparsely studied, with only a few databases available. These databases are expanding rapidly and are critical to the discovery of new 2D crystal properties for practical applications. Below we review the application of advanced machine learning (ML) methods to the modelling and prediction of van der Waals properties that leverage and augment the still relatively small number of experiments on these materials.

With the discovery of many novel 2D crystals, (although experimental synthesis remains challenging), traditional quantum-chemical simulations to predict their properties face two main problems:

- 1) The number of possible heterostructures built using the currently known monolayers (approximately

6,000) becomes unmanageable, as the combinations of two monolayers creates approximately 20 million bilayers, and the number of three-layer combinations reach the trillions.<sup>129, 130</sup> The large computational time and resources required to simulate each heterostructure using quantum chemical or molecular dynamics methods makes modelling this number of structures intractable.

- 2) Many properties, where non-linear effects for a certain regime become dominant, could add a large degree of complexity to each calculation.<sup>131</sup>

Consequently, data driven ML methods have become the dominant means for modelling and predicting the properties of 2D crystals and materials in general.<sup>132</sup> These methods have clearly demonstrated their utility in situations where physics-based simulations for generating physical properties data are not feasible.<sup>133</sup> For example, using data-driven ML methods the properties of over 1.7 million bilayers built from 1800 2D blocks can be predicted.<sup>134</sup>

Structural optimizations and static calculations allow us to determine two of the most important properties that influence the fabrication of novel 2D crystals: the exfoliation energy and the decomposition energy of the material. The exfoliation energy is the average energy per atom that is required for the removal of the layer from the bulk material. The decomposition energy is the energy required for the separation of the materials into elemental components. The few databases that store structural and functional information of 2D crystals are listed in Table 2.

It has been estimated that there are >2000 possible 2D crystals, which combinatorially multiplies the number of possible homo- and hetero-structures. However, only a handful of 2D crystals have been successfully synthesized or exfoliated. The very large majority of 2D crystals have been described only by computational methods, accelerating materials screening by combining complementary methods such as DFT with ML.<sup>135, 136</sup>

Traditional quantum chemical computational techniques such as DFT are widely used for material prediction (e.g., the Materials Genome Project). These techniques can predict many properties of novel and conventional materials with good accuracy. As we stated above, they are very time and resource intensive and models resembling realistic conditions require either a large number of atoms or a long time scales. Large-scale DFT calculations are very time consuming and often scale poorly with system size, typically  $O(N_e^3)$ , with  $N_e$  being the number of Kohn–Sham orbitals.<sup>137, 138</sup> The fastest approach scales as  $O(N)$ , spending most time forming the Hamiltonian and self-consistently solving for the ground state electron eigenstates, a challenging task for large structures with limited periodicity.<sup>139-</sup>

<sup>141</sup> Indeed, such methods are still under development. Semi-empirical approximations to DFT (whilst very promising) introduce approximations that substantially reduce computational time but can be inefficient and/or inaccurate for high-throughput electronic structure screening purposes.<sup>142-144</sup> To improve the accuracy, the semi-empirical parameters need to be developed for each studied case, and currently the computational time saved in the DFT calculation is lost in developing the semi-empirical parameters.<sup>142-144</sup>

However, by exploiting smart synergies between DFT and ML, fast and accurate computational screening of materials of technological interest can be achieved. ML is the general term assigned to all methods that automate analytical model building.<sup>145, 146</sup> ML uses algorithms that iteratively learn from available data and allow computers to find hidden relationships among available parameters, without the use of any explicit formulation of relationships. ML approaches have taken material sciences to a new level and ML-assisted methods have gained huge popularity for a wide range of materials science applications. A major benefit of ML is the increased speed with which solutions for problems in the material sciences can be achieved.<sup>147-150</sup>

ML identifies relationships between the properties of molecules or materials, and structural or physicochemical descriptors (mathematical entities encoding these properties), using minimal computer resources. ML models are data driven; therefore, the quality and range of predictions are critically dependent on the amount, quality, and diversity of data used to train them.

Latent and often nonlinear relationships between the structures, encoded directly or indirectly using a potentially large number of descriptors, and properties of interest are established using ML methods.<sup>150</sup> The generation of large molecule or materials databases is not new, as repositories of experimental data (e.g., Cambridge Structural Database and the Protein Data Bank) have existed for decades.<sup>124, 151</sup> Critically, ML has made it possible to exploit large database of structures and properties to extract information and meaning from these large sets of very complex data.

For example, Tawfik *et al.*<sup>129</sup> employed a variety of ML approaches, including feedforward neural networks, random forests, relevance vector machines, and support vector machines, to predict two important structural and electronic properties of van der Waal heterostructures, the interlayer distance and band gap. Using a similar approach, Fronzi *et al.*<sup>130</sup> built a database for a very large set of heterostructures (18 M), identifying their interlayer energy and elastic constant.

**Table 2.** Materials databases of machine learning on 2D crystals.<sup>152-155</sup>

Database	Number of 2D monolayers	Structural Discovery	Methodological Analysis	Structural derivations
2DMatPedia	~6000	yes	frozen-core all-electron projector-augmented wave (PAW) method	topology-based algorithm and theoretically exfoliated them into monolayers
materialscloud	~400		DFT-PBE van der Waals functionals (rVV10 and DF2-C09)	
C2DB	~4000	yes	GOW0 and the Bethe-Salpeter Equation	geometric analysis, we propose a simple scoring parameter to identify materials of a particular dimension
materialsweb	~800	Yes	plane-wave projector augmented wave method	topology-scaling algorithm

### a. Review of Machine Learning in Materials Discovery

In general, ML models require the existence of suitable training data and the existence of an unknown, often highly non-linear relationship between microscopic or physicochemical properties of materials and measurable and useful macroscopic properties. In supervised ML, the dataset consists of features that describe the structure and corresponding target properties of the structure.<sup>156</sup> The ML algorithms are universal approximators that can, in principle, model any continuous relationship given sufficient data. These algorithms map features to targets, allowing the features of new materials to predict target properties for them, provided they lie close to the domain of the training set.<sup>140</sup> Unsupervised ML methods find neighbourhood relationships between materials and cluster them into classes based on similarity.<sup>157</sup>

Synergistic application of unsupervised and supervised methods has been successful for both materials discovery and characterization. In particular, these approaches have been applied broadly to understand and predict 2D crystals<sup>158</sup>—from understanding complex relationships between the properties and electronic structure, to optimizing structural designs,<sup>159</sup> to the *de novo* discovery of novel structures.<sup>160</sup>

The search through large numbers of candidate materials for novel 2D crystal discovery can also be couched as a global optimization problem; that is, a set of optimization algorithms that do not necessarily require knowledge of existing 2D or bulk crystal structures. These searches, however, generally require hundreds of thousands of function evaluations. Paul *et al.*<sup>161</sup> used genetic algorithms to reduce the number of evaluations, and thereby decrease the computational burden of studying a very large number of candidate materials. Evolutionary algorithms are also efficient ways of exploring the vast space of possible materials that are synthetically accessible.<sup>162</sup>

Taracık *et al.*<sup>159</sup> also used genetic algorithms combined with molecular dynamics (MD) simulations to study point defects and their dynamics, specifically in MoS<sub>2</sub>. The genetic algorithms optimized the structural model of the material. Their work

elucidated the mechanisms that drive the material's semiconducting phase transformations.

A new ground state for 2D TiO<sub>2</sub> was discovered *via* a structural search aided by an artificial neural network.<sup>163</sup> The discovery is an early proof that ML-augmented searches can generate novel results. This newly discovered 2D sheet is predicted to be mechanically and chemically stable. Evolutionary algorithms are also applicable to the prediction of stable atomic structures for material studies, such as predicting current 2D crystals and their low energy states.<sup>164</sup>

Other directed searches have also been conducted by ML.<sup>165</sup> Singh *et al.*<sup>165</sup> searched the 2D group-IV dioxides for useful properties. Using a genetic algorithm, a new low-energy structure with unique symmetry was discovered for 2D germanium oxide (GeO<sub>2</sub>). These findings pave the way to new research directions for applied 2D crystals.

### b. Machine Learning for Piezoelectricity and Non-Linear Effects

One of the most useful applications of ML is in predicting the responses of materials to electric fields and mechanical strain. To predict these responses at scale, dielectric and piezoelectric properties were modelled with a combination of high-throughput density functional perturbation theory and ML.<sup>166, 167</sup>

Linear piezoelectric parameters of the material can be determined *via* well-established approaches, while formulation and measurements of higher-order piezoelectric coefficients (elaststriction and electrostriction) are poorly represented in the literature. Several approaches can be used; however, the accuracy of some of these approaches is limited due to the simplifications used. One example of non-linearity in the response function is that second-order piezoelectric coefficients are finite strain measure dependent.<sup>168</sup>

Dłuzewski *et al.*<sup>169</sup>, using a DFT approach, calculated these properties as a function of strain. The authors observed nonlinear effects under extreme strain. Proper conversion

between deformation and strain is a key issue for the precise measurement or prediction of piezoelectric coefficients. Unfortunately, the strain problem is generally underappreciated. In addition, theoretical studies of the nonlinear elasticity show that third-order stiffness coefficients are strain measurement dependent. This suggests that high-order piezoelectric coefficients also depend on the strain measurement. Thus, nonlinear constitutive equations for piezoelectric materials, and values of the elastic and piezoelectric coefficients, must be consistent. It is important to avoid generating misleading results from the distribution of piezoelectric fields when generating nonlinear modelling of piezoelectric crystals, such as epitaxial heterostructures.<sup>168</sup>

The traditional way of modelling piezoelectricity assumes the interaction between elastic and electric fields is linear.<sup>170</sup> While this classical model can provide suitable results, in some cases, especially for heterostructures under extreme strain and electric field conditions, a significant deviation of the piezoelectric effect from linearity is observed.<sup>171-175</sup>

The interplay of geometric and physical nonlinearity may cause unexpected consequences. For example, the second order piezoelectric coefficients of GaN and GaAs crystals exhibit variation in common strain measures. There is no clear trend, while the average change of the second-order coefficient is around 5%, similar to the measurement uncertainty or precision of the theoretical calculations.<sup>168</sup> Some of the coefficients are strain measure-invariant and for some elastostriction components, the variation reaches a relatively high 20%.

It is predicted that continued experimental research into heterostructures will rapidly accelerate the feasibility of ML approaches, as these can provide critical training set data for more accurate, ML predictions. It should be noted, that heterostructures are complicated for use as a training set, as

minute changes in interface, twist angle, and strain can lead to dramatically different properties. This is further complicated when considering that experimental epitaxial heterostructure synthesis is often achieved at high temperatures and cooling rates, can play a significant and under-reported role in the detailed properties of the heterostructure.

In principle, ML approaches coupled to optimization methods can accelerate the discovery of new piezoelectric materials with large electrostrain properties. Active learning approaches that balance exploration (using uncertainties) and exploitation (using only model predictions) provide an optimal criterion for guiding experiments in materials design.

## 5. Outlook & Conclusions

Piezoelectricity in 2D crystals offers great promise in a diverse range of applications from pressure sensors, energy harvesters, and capacitors. The state of the field is a challenge to assess, due to the lack of standardisation of testing protocols,<sup>176</sup> conflation with triboelectric effects,<sup>11</sup> and diverse terminology used across different fields of science and engineering. Research into piezoelectric energy harvesters or 'nano-generators' in particular is moving so fast it is near impossible to accurately assess any single advance or development in understanding before another, often contradictory, claim emerges.<sup>99, 100</sup> Although beyond the scope of this review, characterizing nanoscale piezoelectricity is of prime importance as clearly discussed by Falconi.<sup>177</sup> As the author correctly highlights, modelling and experimental characterization need to be refined, as crude definition of the geometric shapes of nanomaterials have a dramatic effect on the reported piezoelectric coefficients.<sup>177</sup>

Nevertheless, the outlook for the field overall is particularly bright. Numerous strategies for inducing piezoelectricity in 2D crystals, including defect engineering,<sup>99, 100</sup> elemental

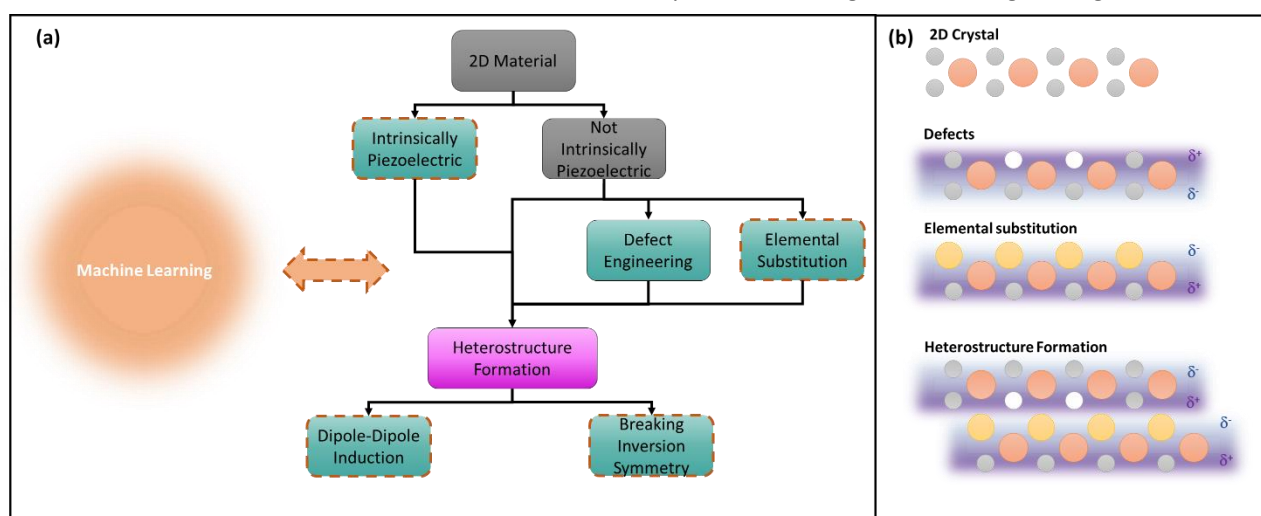


**Figure 15.** Summary of considerations for piezoelectric 2D crystals; a) flowchart highlighting the numerous ways in which piezoelectric output from 2D crystals can be achieved, with machine learning being a powerful tool to predict piezoelectric output in many systems; and b) chemical schematic of how piezoelectricity can be produced or enhanced in a non-intrinsically piezoelectric 2D crystal.

substitution,<sup>104</sup> dipole-dipole induction,<sup>86</sup> and breaking of inversion symmetry are moving from conception to experimental validation very quickly. Use of advanced machine learning tools to predict band-offsets (dipole-dipole interactions), heterostructure unit cells (inversion symmetry), and piezoelectric coefficients from elemental substitution (Figure 15) will further increase the pace of discoveries in this field.

The recent advances in inducing piezoelectricity in materials that lack intrinsic piezoelectric properties have suggested that high performance is possible in most 2D crystals, with the appropriate processing. The question of which 2D crystal is appropriate for device applications thus comes down to the following factors:

- 1) the intrinsic difference in electronegativity of atoms in the unit cell that defines the magnitude of any piezoelectric response (i.e., Mo–Te has a much larger difference than Mo–S);
- 2) the environmental and health impacts of a chosen 2D piezoelectric material e.g.,  $\text{In}_2\text{Se}_3$  is toxic, as are lead-based perovskites, and should be avoided where possible;
- 3) the ease and cost (both financial and energetically) of synthesis; naturally occurring minerals that can be solution phase exfoliated present a more promising large-scale approach;
- 4) complementary materials properties (i.e., catalytic performance, chemical stability, mechanical strength).

By considering these factors, the best 2D crystal for a given application can be chosen, engineered, and integrated into a device, enabling the transition from lab-based to practical 2D crystal piezoelectric devices to finally be realized at scale.

## 6. Author Contributions

Conceptualisation: PCS, MF, NAS, AC, DW, MF, JGS, AVE; Funding Acquisition: DW, MF, JGS, AVE; Supervision: DW, MF, JGS, AVE; Visualisation: PCS, NAS, AC; Writing – Original Draft: PCS, MF, NAS, AC, JGS; Writing – Review & Editing: PCS; MF; NAS; AC; DW; MF; JGS; AVE

## 7. Conflicts of interest

There are no conflicts to declare

## 8. Acknowledgements

The authors gratefully acknowledge the financial support of Australian Government through the Australian Research Council (ARC DP200101217).

PCS acknowledges support through the Elizabeth & Vernon Puzey Foundation.

## Notes and references

1. X. Zhuang, B. He, B. Javvaji and H. S. Park, *Physical Review B*, 2019, **99**, 054105.
2. S. Chandratre and P. Sharma, *Applied Physics Letters*, 2012, **100**, 023114.
3. M. Noor-A-Alam, H. J. Kim and Y.-H. Shin, *Physical Chemistry Chemical Physics*, 2014, **16**, 6575–6582.
4. J.-H. Lee, J. Y. Park, E. B. Cho, T. Y. Kim, S. A. Han, T.-H. Kim, Y. Liu, S. K. Kim, C. J. Roh, H.-J. Yoon, H. Ryu, W. Seung, J. S. Lee, J. Lee and S.-W. Kim, *Advanced Materials*, 2017, **29**, 1606667.
5. K. Novoselov, o. A. Mishchenko, o. A. Carvalho and A. C. Neto, *Science*, 2016, **353**.
6. L. Lin, P. Sherrell, Y. Liu, W. Lei, S. Zhang, H. Zhang, G. G. Wallace and J. Chen, *Advanced Energy Materials*, 2020, **10**, 1903870.
7. X.-P. Zhai, B. Ma, Q. Wang and H.-L. Zhang, *Physical Chemistry Chemical Physics*, 2020, **22**, 22140–22156.
8. M. B. Ghasemian, T. Daeneke, Z. Shahrababaki, J. Yang and K. Kalantar-Zadeh, *Nanoscale*, 2020, **12**, 2875–2901.
9. D. Damjanovic, *Reports on Progress in Physics*, 1998, **61**, 1267–1324.
10. N. A. Shepelin, P. C. Sherrell, E. N. Skountzos, E. Goudeli, J. Zhang, V. C. Lussini, B. Imtiaz, K. A. S. Usman, G. W. Dicoski, J. G. Shapter, J. M. Razal and A. V. Ellis, *Nature Communications*, 2021, **12**, 3171.
11. A. Šutka, P. C. Sherrell, N. A. Shepelin, L. Lapčinskis, K. Mālnieks and A. V. Ellis, *Advanced Materials*, 2020, **32**, 2002979.
12. R. Shaltaf, E. Durgun, J. Y. Raty, P. Ghosez and X. Gonze, *Physical Review B*, 2008, **78**, 205203.
13. M. Zelisko, Y. Hanlumyuang, S. Yang, Y. Liu, C. Lei, J. Li, P. M. Ajayan and P. Sharma, *Nature Communications*, 2014, **5**, 4284.
14. K.-A. N. Duerloo, M. T. Ong and E. J. Reed, *The Journal of Physical Chemistry Letters*, 2012, **3**, 2871–2876.
15. C. Tan, J. Chen, X.-J. Wu and H. Zhang, *Nature Reviews Materials*, 2018, **3**, 17089.
16. Y. Gong, J. Lin, X. Wang, G. Shi, S. Lei, Z. Lin, X. Zou, G. Ye, R. Vajtai, B. I. Yakobson, H. Terrones, M. Terrones, Beng K. Tay, J. Lou, S. T. Pantelides, Z. Liu, W. Zhou and P. M. Ajayan, *Nature Materials*, 2014, **13**, 1135–1142.
17. A. Weston, Y. Zou, V. Enaldiev, A. Summerfield, N. Clark, V. Zólyomi, A. Graham, C. Yelgel, S. Magorrian, M. Zhou, J. Zultak, D. Hopkinson, A. Barinov, T. H. Bointon, A. Kretinin, N. R. Wilson, P. H. Beton, V. I. Fal'ko, S. J. Haigh and R. Gorbachev, *Nature Nanotechnology*, 2020, **15**, 592–597.
18. X. Song, F. Hui, T. Knobloch, B. Wang, Z. Fan, T. Grasser, X. Jing, Y. Shi and M. Lanza, *Applied Physics Letters*, 2017, **111**, 083107.
19. X. Wang, H. Tian, W. Xie, Y. Shu, W.-T. Mi, M. Ali Mohammad, Q.-Y. Xie, Y. Yang, J.-B. Xu and T.-L. Ren, *NPG Asia Materials*, 2015, **7**, e154–e154.
20. M. T. Ong and E. J. Reed, *ACS nano*, 2012, **6**, 1387–1394.
21. A. Carvalho, M. Wang, X. Zhu, A. S. Rodin, H. Su and A. H. Castro Neto, *Nature Reviews Materials*, 2016, **1**, 16061.
22. L. Drissi, S. Sadki and K. Sadki, *Journal of Physics and Chemistry of Solids*, 2018, **112**, 137–142.
23. W. Li and J. Li, *Nano Research*, 2015, **8**, 3796–3802.
24. H. Yin, G.-P. Zheng, J. Gao, Y. Wang and Y. Ma, *Physical Chemistry Chemical Physics*, 2017, **19**, 27508–27515.

25. M. Noor-A-Alam, H. J. Kim and Y.-H. Shin, *Journal of Applied Physics*, 2015, **117**, 224304.
26. Z. Chang, W. Yan, J. Shang and J. Z. Liu, *Applied Physics Letters*, 2014, **105**, 023103.
27. M. N. Blonsky, H. L. Zhuang, A. K. Singh and R. G. Hennig, *ACS nano*, 2015, **9**, 9885-9891.
28. Y. Guo, S. Zhou, Y. Bai and J. Zhao, *Applied Physics Letters*, 2017, **110**, 163102.
29. L. Li, H. Cao, B. Xu, J. Deng, J. Liu, Y. Liu, X. Ding, J. Sun and J. Z. Liu, *Physical Review Applied*, 2020, **13**, 054061.
30. Z. Li, C. He, T. Ouyang, C. Zhang, C. Tang, R. A. Römer and J. Zhong, *Physical Review Applied*, 2018, **9**, 044032.
31. J. Li, T. Zhao, C. He and K. Zhang, *Journal of Physics D: Applied Physics*, 2018, **51**, 12LT01.
32. A. Ziletti, A. Carvalho, P. E. Trevisanutto, D. K. Campbell, D. F. Coker and A. H. Castro Neto, *Physical Review B*, 2015, **91**, 085407.
33. J. R. Reimers, S. A. Tawfik and M. J. Ford, *Chemical Science*, 2018, **9**, 7620-7627.
34. P. Ares, T. Cea, M. Holwill, Y. B. Wang, R. Roldán, F. Guinea, D. V. Andreeva, L. Fumagalli, K. S. Novoselov and C. R. Woods, *Advanced Materials*, 2020, **32**, 1905504.
35. W. Ma, J. Lu, B. Wan, D. Peng, Q. Xu, G. Hu, Y. Peng, C. Pan and Z. L. Wang, *Advanced Materials*, 2020, **32**, 1905795.
36. K. Jenkins, V. Nguyen, R. Zhu and R. Yang, *Sensors (Basel)*, 2015, **15**, 22914-22940.
37. D. R. Kripalani, A. A. Kistanov, Y. Cai, M. Xue and K. Zhou, *Physical Review B*, 2018, **98**, 085410.
38. P. Jamdagni, A. Thakur, A. Kumar, P. K. Ahluwalia and R. Pandey, *The Journal of Physical Chemistry C*, 2019, **123**, 27214-27221.
39. H. Lu, J. Gao, Z. Hu and X. Shao, *RSC Advances*, 2016, **6**, 102724-102732.
40. T. T. Tran, K. Bray, M. J. Ford, M. Toth and I. Aharonovich, *Nature nanotechnology*, 2016, **11**, 37-41.
41. H. Momida and T. Oguchi, *Applied Physics Express*, 2018, **11**, 041201.
42. L. Bellaïche and D. Vanderbilt, *Physical review letters*, 1999, **83**, 1347.
43. M. M. Alyörük, *physica status solidi (b)*, 2016, **253**, 2534-2539.
44. A. Zavabeti, J. Z. Ou, B. J. Carey, N. Syed, R. Orrell-Trigg, E. L. H. Mayes, C. Xu, O. Kavehei, A. P. O'Mullane, R. B. Kaner, K. Kalantar-zadeh and T. Daeneke, *Science*, 2017, **358**, 332.
45. P. Kumbhakar, C. Chowde Gowda, P. L. Mahapatra, M. Mukherjee, K. D. Malviya, M. Chaker, A. Chandra, B. Lahiri, P. M. Ajayan, D. Jariwala, A. Singh and C. S. Tiwary, *Materials Today*, 2021, **45**, 142-168.
46. M. B. Ghasemian, A. Zavabeti, R. Abbasi, P. V. Kumar, N. Syed, Y. Yao, J. Tang, Y. Wang, A. Elbourne, J. Han, M. Mousavi, T. Daeneke and K. Kalantar-Zadeh, *Journal of Materials Chemistry A*, 2020, **8**, 19434-19443.
47. R. Fei, W. Li, J. Li and L. Yang, *Applied Physics Letters*, 2015, **107**, 173104.
48. Y. Guo, S. Zhou, Y. Bai and J. Zhao, *ACS Applied Materials & Interfaces*, 2017, **9**, 12013-12020.
49. H. Khan, N. Mahmood, A. Zavabeti, A. Elbourne, M. A. Rahman, B. Y. Zhang, V. Krishnamurthi, P. Atkin, M. B. Ghasemian, J. Yang, G. Zheng, A. R. Ravindran, S. Walia, L. Wang, S. P. Russo, T. Daeneke, Y. Li and K. Kalantar-Zadeh, *Nature Communications*, 2020, **11**, 3449.
50. L. C. Gomes, A. Carvalho and A. C. Neto, *Physical Review B*, 2015, **92**, 214103.
51. M. M. Alyörük, Y. Aierken, D. Çakır, F. M. Peeters and C. Sevik, *The Journal of Physical Chemistry C*, 2015, **119**, 23231-23237.
52. M. S. Sokolikova, P. C. Sherrell, P. Palczynski, V. L. Bemmer and C. Mattevi, *Nature Communications*, 2019, **10**, 712.
53. M. M. Ugeda, A. Pulkin, S. Tang, H. Ryu, Q. Wu, Y. Zhang, D. Wong, Z. Pedramrazi, A. Martín-Recio, Y. Chen, F. Wang, Z.-X. Shen, S.-K. Mo, O. V. Yazyev and M. F. Crommie, *Nature Communications*, 2018, **9**, 3401.
54. W. Chen, X. Xie, J. Zong, T. Chen, D. Lin, F. Yu, S. Jin, L. Zhou, J. Zou, J. Sun, X. Xi and Y. Zhang, *Scientific Reports*, 2019, **9**, 2685.
55. J. Q. Geisenhoff, A. K. Tamura and A. M. Schimpf, *Chemical Communications*, 2019, **55**, 8856-8859.
56. M. Tannarana, G. K. Solanki, S. A. Bhakhar, K. D. Patel, V. M. Pathak and P. M. Pataniya, *ACS Sustainable Chemistry & Engineering*, 2020, **8**, 7741-7749.
57. Y. Wang, L.-M. Vu, T. Lu, C. Xu, Y. Liu, J. Z. Ou and Y. Li, *ACS Applied Materials & Interfaces*, 2020, **12**, 51662-51668.
58. M. S. Sokolikova and C. Mattevi, *Chemical Society Reviews*, 2020, **49**, 3952-3980.
59. B. Anasori, M. R. Lukatskaya and Y. Gogotsi, *Nature Reviews Materials*, 2017, **2**, 16098.
60. R. Wang, M. Mujahid, Y. Duan, Z.-K. Wang, J. Xue and Y. Yang, *Advanced Functional Materials*, 2019, **29**, 1808843.
61. C. W. Jang, H. Kim, M. K. Nazeeruddin, D. H. Shin and S.-H. Choi, *Nano Energy*, 2021, **84**, 105899.
62. D. D. Fong, G. B. Stephenson, S. K. Streiffer, J. A. Eastman, O. Auciello, P. H. Fuoss and C. Thompson, *Science*, 2004, **304**, 1650.
63. D. D. Fong, G. B. Stephenson, S. K. Streiffer, J. A. Eastman, O. Auciello, P. H. Fuoss and C. Thompson, *Science*, 2004, **304**, 1650-1653.
64. A. Gruverman, D. Wu, H. Lu, Y. Wang, H. W. Jang, C. M. Folkman, M. Y. Zhuravlev, D. Felker, M. Rzchowski, C. B. Eom and E. Y. Tsybal, *Nano Letters*, 2009, **9**, 3539-3543.
65. W. Jin Hu, Z. Wang, W. Yu and T. Wu, *Nature Communications*, 2016, **7**, 10808.
66. C. Cui, F. Xue, W.-J. Hu and L.-J. Li, *npj 2D Materials and Applications*, 2018, **2**, 18.
67. K. Leng, W. Fu, Y. Liu, M. Chhowalla and K. P. Loh, *Nature Reviews Materials*, 2020, **5**, 482-500.
68. L. You, F. Liu, H. Li, Y. Hu, S. Zhou, L. Chang, Y. Zhou, Q. Fu, G. Yuan, S. Dong, H. J. Fan, A. Gruverman, Z. Liu and J. Wang, *Advanced Materials*, 2018, **30**, 1803249.
69. S. S. Cheema, D. Kwon, N. Shanker, R. dos Reis, S.-L. Hsu, J. Xiao, H. Zhang, R. Wagner, A. Datar, M. R. McCarter, C. R. Serrao, A. K. Yadav, G. Karbasian, C.-H. Hsu, A. J. Tan, L.-C. Wang, V. Thakare, X. Zhang, A. Mehta, E. Karapetrova, R. V. Chopdekar, P. Shafer, E. Arenholz, C. Hu, R. Proksch, R. Ramesh, J. Ciston and S. Salahuddin, *Nature*, 2020, **580**, 478-482.
70. J. Nordlander, M. D. Rossell, M. Campanini, M. Fiebig and M. Trassin, *Nano Letters*, 2021, **21**, 2780-2785.
71. L. Qi, S. Ruan and Y.-J. Zeng, *Advanced Materials*, 2021, **33**, 2005098.
72. G. Monastyreckis, L. Mishnaevsky, C. B. Hatter, A. Aniskevich, Y. Gogotsi and D. Zeleniakiene, *Carbon*, 2020, **162**, 402-409.

73. F. Shahzad, M. Alhabeab, C. B. Hatter, B. Anasori, S. Man Hong, C. M. Koo and Y. Gogotsi, *Science*, 2016, **353**, 1137.
74. J. Tan, Y. Wang, Z. Wang, X. He, Y. Liu, B. Wang, M. I. Katsnelson and S. Yuan, *Nano Energy*, 2019, **65**, 104058.
75. J. Gu, Z. Zhao, J. Huang, B. G. Sumpter and Z. Chen, *ACS Nano*, 2021, **15**, 6233-6242.
76. Y. Zhou, D. Wu, Y. Zhu, Y. Cho, Q. He, X. Yang, K. Herrera, Z. Chu, Y. Han, M. C. Downer, H. Peng and K. Lai, *Nano Letters*, 2017, **17**, 5508-5513.
77. F. Xue, J. Zhang, W. Hu, W.-T. Hsu, A. Han, S.-F. Leung, J.-K. Huang, Y. Wan, S. Liu, J. Zhang, J.-H. He, W.-H. Chang, Z. L. Wang, X. Zhang and L.-J. Li, *ACS Nano*, 2018, **12**, 4976-4983.
78. F. Liu, L. You, K. L. Seyler, X. Li, P. Yu, J. Lin, X. Wang, J. Zhou, H. Wang and H. He, *Nature communications*, 2016, **7**, 1-6.
79. D. M. Kim, C.-B. Eom, V. Nagarajan, J. Ouyang, R. Ramesh, V. Vaithyanathan and D. G. Schlom, *Applied physics letters*, 2006, **88**, 142904.
80. H. Yin, G.-P. Zheng, Y. Wang and B. Yao, *Physical Chemistry Chemical Physics*, 2018, **20**, 19177-19187.
81. F. M. Pesci, M. S. Sokolikova, C. Grotta, P. C. Sherrell, F. Reale, K. Sharda, N. Ni, P. Palczynski and C. Mattevi, *ACS Catalysis*, 2017, **7**, 4990-4998.
82. P. C. Sherrell, P. Palczynski, M. S. Sokolikova, F. Reale, F. M. Pesci, M. Och and C. Mattevi, *ACS Applied Energy Materials*, 2019, **2**, 5877-5882.
83. M. K. Mohanta, A. Rawat, Dimple, N. Jena, R. Ahammed and A. De Sarkar, *Nanoscale*, 2019, **11**, 21880-21890.
84. M. K. Mohanta and A. De Sarkar, *Nanoscale*, 2020, **12**, 22645-22657.
85. M. K. Mohanta, A. Rawat, N. Jena, Dimple, R. Ahammed and A. De Sarkar, *ACS Applied Materials & Interfaces*, 2020, **12**, 3114-3126.
86. S. Yuan, W. F. Io, J. Mao, Y. Chen, X. Luo and J. Hao, *ACS Applied Nano Materials*, 2020, **3**, 11979-11986.
87. L. Huang, Y. Li, Z. Wei and J. Li, *Scientific reports*, 2015, **5**, 1-7.
88. J. L. Zhang, S. Zhao, C. Han, Z. Wang, S. Zhong, S. Sun, R. Guo, X. Zhou, C. D. Gu and K. D. Yuan, *Nano letters*, 2016, **16**, 4903-4908.
89. X. Li, X. Wang, W. Hao, C. Mi and H. Zhou, *AIP Advances*, 2019, **9**, 115302.
90. K. Yasuda, X. Wang, K. Watanabe, T. Taniguchi and P. Jarillo-Herrero, *Science*, 2021, **372**, 1458-1462.
91. C. R. Woods, P. Ares, H. Nevison-Andrews, M. J. Holwill, R. Fabregas, F. Guinea, A. K. Geim, K. S. Novoselov, N. R. Walet and L. Fumagalli, *Nature Communications*, 2021, **12**, 347.
92. M. Vizner Stern, Y. Waschitz, W. Cao, I. Nevo, K. Watanabe, T. Taniguchi, E. Sela, M. Urbakh, O. Hod and M. Ben Shalom, *Science*, 2021, **372**, 1462-1466.
93. Z. Zheng, Q. Ma, Z. Bi, S. de la Barrera, M.-H. Liu, N. Mao, Y. Zhang, N. Kiper, K. Watanabe, T. Taniguchi, J. Kong, W. A. Tisdale, R. Ashoori, N. Gedik, L. Fu, S.-Y. Xu and P. Jarillo-Herrero, *Nature*, 2020, **588**, 71-76.
94. L. J. McGilly, A. Kerelsky, N. R. Finney, K. Shapovalov, E.-M. Shih, A. Ghiotto, Y. Zeng, S. L. Moore, W. Wu, Y. Bai, K. Watanabe, T. Taniguchi, M. Stengel, L. Zhou, J. Hone, X. Zhu, D. N. Basov, C. Dean, C. E. Dreyer and A. N. Pasupathy, *Nature Nanotechnology*, 2020, **15**, 580-584.
95. Y. Li, X. Wang, D. Tang, X. Wang, K. Watanabe, T. Taniguchi, D. R. Gamelin, D. H. Cobden, M. Yankowitz, X. Xu and J. Li, *Advanced Materials*, **n/a**, 2105879.
96. S. Krichen and P. Sharma, *Journal of Applied Mechanics*, 2016, **83**.
97. S. Kang, S. Kim, S. Jeon, W.-S. Jang, D. Seol, Y.-M. Kim, J. Lee, H. Yang and Y. Kim, *Nano Energy*, 2019, **58**, 57-62.
98. W. Choi, J. Kim, E. Lee, G. Mehta and V. Prasad, *ACS Applied Materials & Interfaces*, 2021, **13**, 13596-13603.
99. A. Apte, K. Mozaffari, F. S. Samghabadi, J. A. Hachtel, L. Chang, S. Susarla, J. C. Idrobo, D. C. Moore, N. R. Glavin, D. Litvinov, P. Sharma, A. B. Puthirath and P. M. Ajayan, *Advanced Materials*, 2020, **32**, 2000006.
100. S. A. Han, T.-H. Kim, S. K. Kim, K. H. Lee, H.-J. Park, J.-H. Lee and S.-W. Kim, *Advanced Materials*, 2018, **30**, 1800342.
101. Y. C. Cheng, Z. Y. Zhu, M. Tahir and U. Schwingenschlöggl, *EPL (Europhysics Letters)*, 2013, **102**, 57001.
102. A.-Y. Lu, H. Zhu, J. Xiao, C.-P. Chuu, Y. Han, M.-H. Chiu, C.-C. Cheng, C.-W. Yang, K.-H. Wei, Y. Yang, Y. Wang, D. Sokaras, D. Nordlund, P. Yang, D. A. Muller, M.-Y. Chou, X. Zhang and L.-J. Li, *Nature Nanotechnology*, 2017, **12**, 744-749.
103. J. Zhang, S. Jia, I. Kholmanov, L. Dong, D. Er, W. Chen, H. Guo, Z. Jin, V. B. Shenoy, L. Shi and J. Lou, *ACS Nano*, 2017, **11**, 8192-8198.
104. L. Dong, J. Lou and V. B. Shenoy, *ACS Nano*, 2017, **11**, 8242-8248.
105. J. Qiu, H. Li, X. Chen, B. Zhu, H. Guo, F. Zhang, Z. Ding, L. Lang, J. Yu and J. Bao, *Journal of Applied Physics*, 2021, **129**, 125109.
106. Y. Chen, J. Liu, J. Yu, Y. Guo and Q. Sun, *Physical Chemistry Chemical Physics*, 2019, **21**, 1207-1216.
107. P. Nandi, A. Rawat, R. Ahammed, N. Jena and A. De Sarkar, *Nanoscale*, 2021, **13**, 5460-5478.
108. Z. Kahraman, A. Kandemir, M. Yagmurcukardes and H. Sahin, *The Journal of Physical Chemistry C*, 2019, **123**, 4549-4557.
109. S.-D. Guo, X.-S. Guo, Z.-Y. Liu and Y.-N. Quan, *Journal of Applied Physics*, 2020, **127**, 064302.
110. R. Ahammed, N. Jena, A. Rawat, M. K. Mohanta, Dimple and A. De Sarkar, *The Journal of Physical Chemistry C*, 2020, **124**, 21250-21260.
111. Dimple, N. Jena, A. Rawat, R. Ahammed, M. K. Mohanta and A. De Sarkar, *Journal of Materials Chemistry A*, 2018, **6**, 24885-24898.
112. P. C. Sherrell, K. Sharda, C. Grotta, J. Ranalli, M. S. Sokolikova, F. M. Pesci, P. Palczynski, V. L. Bemmer and C. Mattevi, *ACS Omega*, 2018, **3**, 8655-8662.
113. H. Nam, H. Yang, E. Kim, C. Bae and H. Shin, *Journal of Vacuum Science & Technology A*, 2019, **37**, 020916.
114. F. Iyikanat, H. Sahin, R. T. Senger and F. M. Peeters, *The Journal of Physical Chemistry C*, 2015, **119**, 10709-10715.
115. Z. Li, Y. Lv, L. Ren, J. Li, L. Kong, Y. Zeng, Q. Tao, R. Wu, H. Ma, B. Zhao, D. Wang, W. Dang, K. Chen, L. Liao, X. Duan, X. Duan and Y. Liu, *Nature Communications*, 2020, **11**, 1151.
116. P. Zubko, G. Catalan and A. K. Tagantsev, *Annual Review of Materials Research*, 2013, **43**, 387-421.
117. S. V. Kalinin and V. Meunier, *Physical Review B*, 2008, **77**, 033403.
118. D. Lee and T. W. Noh, *Philosophical Transactions of the Royal Society A: Mathematical, Physical and Engineering Sciences*, 2012, **370**, 4944-4957.
119. W. Ma and L. E. Cross, *Applied Physics Letters*, 2002, **81**, 3440-3442.

120. A. Rawat, M. K. Mohanta, N. Jena, Dimple, R. Ahammed and A. De Sarkar, *The Journal of Physical Chemistry C*, 2020, **124**, 10385-10397.
121. K. S. Novoselov, A. K. Geim, S. V. Morozov, D. Jiang, Y. Zhang, S. V. Dubonos, I. V. Grigorieva and A. A. Firsov, *science*, 2004, **306**, 666-669.
122. A. Belsky, M. Hellenbrandt, V. L. Karen and P. Luksch, *Acta Crystallographica Section B*, 2002, **58**, 364-369.
123. S. Kirklın, J. E. Saal, B. Meredig, A. Thompson, J. W. Doak, M. Aykol, S. Rühl and C. Wolverton, *npj Computational Materials*, 2015, **1**, 1-15.
124. F. H. Allen, *Acta Crystallographica Section B: Structural Science*, 2002, **58**, 380-388.
125. J. Hachmann, R. Olivares-Amaya, S. Atahan-Evrenk, C. Amador-Bedolla, R. S. Sánchez-Carrera, A. Gold-Parker, L. Vogt, A. M. Brockway and A. Aspuru-Guzik, *The Journal of Physical Chemistry Letters*, 2011, **2**, 2241-2251.
126. A. Jain, S. P. Ong, G. Hautier, W. Chen, W. D. Richards, S. Dacek, S. Cholia, D. Gunter, D. Skinner and G. Ceder, *APL materials*, 2013, **1**, 011002.
127. B. Puchala, G. Tarcea, E. A. Marquis, M. Hedstrom, H. Jagadish and J. E. Allison, *Jom*, 2016, **68**, 2035-2044.
128. B. Blaiszik, K. Chard, J. Pruyne, R. Ananthakrishnan, S. Tuecke and I. Foster, *Jom*, 2016, **68**, 2045-2052.
129. S. A. Tawfik, O. Isayev, C. Stampfl, J. Shapter, D. A. Winkler and M. J. Ford, *Advanced Theory and Simulations*, 2019, **2**, 1800128.
130. M. Fronzi, S. A. Tawfik, M. A. Ghazaleh, O. Isayev, D. A. Winkler, J. Shapter and M. J. Ford, *Advanced Theory and Simulations*, 2020, **3**, 2000029.
131. J. You, S. Bongu, Q. Bao and N. Panoiu, *Nanophotonics*, 2019, **8**, 63-97.
132. T. Le, V. C. Epa, F. R. Burden and D. A. Winkler, *Chem Rev*, 2012, **112**, 2889-2919.
133. S. Masubuchi, E. Watanabe, Y. Seo, S. Okazaki, T. Sasagawa, K. Watanabe, T. Taniguchi and T. Machida, *npj 2D Materials and Applications*, 2020, **4**, 1-9.
134. F. R. Burden and D. A. Winkler, *Journal of chemical information and modeling*, 2015, **55**, 1529-1534.
135. O. Isayev, C. Oses, C. Toher, E. Gossett, S. Curtarolo and A. Tropsha, *Nature communications*, 2017, **8**, 1-12.
136. M. Fronzi, O. Isayev, D. A. Winkler, J. G. Shapter, A. V. Ellis, P. C. Sherrell, N. A. Shepelin, A. Corletto and M. J. Ford, *Advanced Intelligent Systems*, 2021, **3**, 2100080.
137. P. Hohenberg and W. Kohn, *Physical review*, 1964, **136**, B864.
138. W. Kohn and L. J. Sham, *Physical review*, 1965, **140**, A1133.
139. D. R. Bowler and T. Miyazaki, *Reports on Progress in Physics*, 2012, **75**, 036503.
140. G. Hegde and R. C. Bowen, *Scientific reports*, 2017, **7**, 1-11.
141. S. Goedecker, *Reviews of Modern Physics*, 1999, **71**, 1085.
142. C. Goringe, D. Bowler and E. Hernandez, *Reports on Progress in Physics*, 1997, **60**, 1447.
143. G. Klimeck, R. C. Bowen, T. B. Boykin, C. Salazar-Lazaro, T. A. Cwik and A. Stoica, *Superlattices and Microstructures*, 2000, **27**, 77-88.
144. G. Hegde, M. Povolotskyi, T. Kubis, T. Boykin and G. Klimeck, *Journal of Applied Physics*, 2014, **115**, 123703.
145. M. Ceriotti, *The Journal of chemical physics*, 2019, **150**, 150901.
146. T. M. Mitchell, *Machine learning*, McGraw-Hill, 1997.
147. J. Wei, X. Chu, X. Y. Sun, K. Xu, H. X. Deng, J. Chen, Z. Wei and M. Lei, *InfoMat*, 2019, **1**, 338-358.
148. J. Behler, *The Journal of chemical physics*, 2016, **145**, 170901.
149. B. G. Sumpter, C. Getino and D. W. Noid, *Annual Review of Physical Chemistry*, 1994, **45**, 439-481.
150. J. Gasteiger and J. Zupan, *Angewandte Chemie International Edition in English*, 1993, **32**, 503-527.
151. F. C. Bernstein, T. F. Koetzle, G. J. Williams, E. F. Meyer Jr, M. D. Brice, J. R. Rodgers, O. Kennard, T. Shimanouchi and M. Tasumi, *Archives of biochemistry and biophysics*, 1978, **185**, 584-591.
152. J. Zhou, L. Shen, M. D. Costa, K. A. Persson, S. P. Ong, P. Huck, Y. Lu, X. Ma, Y. Chen, H. Tang and Y. P. Feng, *Scientific Data*, 2019, **6**, 86.
153. N. Mounet, M. Gibertini, P. Schwaller, D. Campi, A. Merkys, A. Marrazzo, T. Sohier, I. E. Castelli, A. Cepellotti, G. Pizzi and N. Marzari, *Nature Nanotechnology*, 2018, **13**, 246-252.
154. S. Haastrup, M. Strange, M. Pandey, T. Deilmann, P. S. Schmidt, N. F. Hinsche, M. N. Gjerding, D. Torelli, P. M. Larsen, A. C. Riis-Jensen, J. Gath, K. W. Jacobsen, J. Jørgen Mortensen, T. Olsen and K. S. Thygesen, *2D Materials*, 2018, **5**, 042002.
155. M. Ashton, J. Paul, S. B. Sinnott and R. G. Hennig, *Physical Review Letters*, 2017, **118**, 106101.
156. A. Singh, N. Thakur and A. Sharma, *2016 3rd International Conference on Computing for Sustainable Global Development (INDIACom)*, 2016, 1310-1315.
157. A. Krizhevsky, I. Sutskever and G. E. Hinton, *Advances in neural information processing systems*, 2012, **25**, 1097-1105.
158. K. Momeni, Y. Ji, Y. Wang, S. Paul, S. Neshani, D. E. Yilmaz, Y. K. Shin, D. Zhang, J.-W. Jiang and H. S. Park, *npj Computational Materials*, 2020, **6**, 1-18.
159. T. K. Patra, F. Zhang, D. S. Schulman, H. Chan, M. J. Cherkar, M. Terrones, S. Das, B. Narayanan and S. K. Sankaranarayanan, *ACS nano*, 2018, **12**, 8006-8016.
160. K. Choudhary, B. DeCost and F. Tavazza, *Physical review materials*, 2018, **2**, 083801.
161. J. Paul, A. Singh, Z. Dong, H. Zhuang, B. Revard, B. Rijal, M. Ashton, A. Linscheid, M. Blonsky and D. Gluhovic, *Journal of Physics: Condensed Matter*, 2017, **29**, 473001.
162. T. C. Le and D. A. Winkler, *Chem Rev*, 2016, **116**, 6107-6132.
163. H. A. Eivari, S. A. Ghasemi, H. Tahmasbi, S. Rostami, S. Faraji, R. Rasoulkhani, S. Goedecker and M. Amsler, *Chemistry of Materials*, 2017, **29**, 8594-8603.
164. W. W. Tipton and R. G. Hennig, *Journal of Physics: Condensed Matter*, 2013, **25**, 495401.
165. A. K. Singh, B. C. Revard, R. Ramanathan, M. Ashton, F. Tavazza and R. G. Hennig, *Physical Review B*, 2017, **95**, 155426.
166. C. Tan, X. Cao, X.-J. Wu, Q. He, J. Yang, X. Zhang, J. Chen, W. Zhao, S. Han, G.-H. Nam, M. Sindoro and H. Zhang, *Chemical Reviews*, 2017, **117**, 6225-6331.
167. C. R. Dean, A. F. Young, I. Meric, C. Lee, L. Wang, S. Sorgenfrei, K. Watanabe, T. Taniguchi, P. Kim, K. L. Shepard and J. Hone, *Nature Nanotechnology*, 2010, **5**, 722-726.
168. G. Jurczak, *Acta Crystallographica Section A: Foundations and Advances*, 2018, **74**, 518-523.
169. P. Dłuzewski, *Journal of elasticity and the physical science of solids*, 2000, **60**, 119-129.

170. J. F. Nye, *Physical properties of crystals: their representation by tensors and matrices*, Oxford university press, 1985.
171. A. D. Andreev and E. P. O'Reilly, *Physical Review B*, 2000, **62**, 15851-15870.
172. H. Beige, *Ferroelectrics*, 1983, **51**, 113-119.
173. V. A. Fonoberov and A. A. Balandin, *Journal of Applied Physics*, 2003, **94**, 7178-7186.
174. G. Dimitrakopoulos, E. Kalesaki, J. Kioseoglou, T. Kehagias, A. Lotsari, L. Lahourcade, E. Monroy, I. Häusler, H. Kirmse and W. Neumann, *Journal of Applied Physics*, 2010, **108**, 104304.
175. G. Jurczak and T. D. Young, *Applied surface science*, 2012, **260**, 59-64.
176. J. Briscoe, N. Jalali, P. Woolliams, M. Stewart, P. M. Weaver, M. Cain and S. Dunn, *Energy & Environmental Science*, 2013, **6**, 3035-3045.
177. C. Falconi, *Nano Energy*, 2019, **59**, 730-744.